Dalton Transactions

RSCPublishing

PERSPECTIVE

View Article Online

Magnetic properties and energy-mapping analysis

Cite this: Dalton Trans., 2013, 42, 823

Hongjun Xiang,*a Changhoon Lee,†b Hyun-Joo Koo,c Xingao Gonga and Myung-Hwan Whangbo*b

The magnetic energy levels of a given magnetic solid are closely packed in energy because the interactions between magnetic ions are weak. Thus, in describing its magnetic properties, one needs to generate its magnetic energy spectrum by employing an appropriate spin Hamiltonian. In this review article we discuss how to determine and specify a necessary spin Hamiltonian in terms of first principles electronic structure calculations on the basis of energy-mapping analysis and briefly survey important concepts and phenomena that one encounters in reading the current literature on magnetic solids. Our discussion is given on a qualitative level from the perspective of magnetic energy levels and electronic structures. The spin Hamiltonian appropriate for a magnetic system should be based on its spin lattice, i.e., the repeat pattern of its strong magnetic bonds (strong spin exchange paths), which requires one to evaluate its Heisenberg spin exchanges on the basis of energy-mapping analysis. Other weaker energy terms such as Dzyaloshinskii-Moriya (DM) spin exchange and magnetocrystalline anisotropy energies, which a spin Hamiltonian must include in certain cases, can also be evaluated by performing energymapping analysis. We show that the spin orientation of a transition-metal magnetic ion can be easily explained by considering its split d-block levels as unperturbed states with the spin-orbit coupling (SOC)

Received 24th July 2012, Accepted 26th September 2012 DOI: 10.1039/c2dt31662e

www.rsc.org/dalton

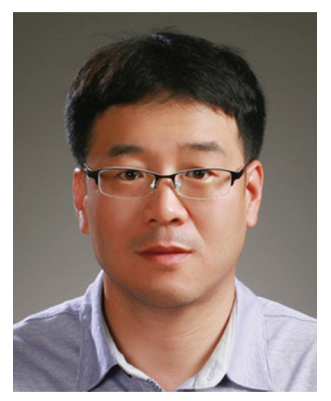
[†]Present address: Department of Chemistry, Pohang University of Science and Technology, Pohang, Kyungbuk 790-784, Korea.



Hongjun Xiang

Hongjun Xiang received his BS and PhD in chemical physics from the University of Science and Technology of China in 2001 and 2006, respectively. He worked on magnetic systems with Professor M.-H. Whangbo at North Carolina State University from September 2006 to August 2007. From August 2007 to December 2009, he stayed at the National Renewable Energy Laboratory where he performed research on energy related

materials. Since October 2009, Hongjun Xiang has been a Professor of Physics at Fudan University. His current research focus is on theoretical studies of multiferroics and on first principles prediction and design of new materials.



Changhoon Lee

Changhoon Lee received his bachelor's and master's degrees from Wonkwang University in 1998 and 2000, respectively. After receiving his PhD in chemistry from Wonkwang University in 2005, he joined Professor M.-H. Whangbo's research group as a postdoctoral associate and subsequently as a research assistant professor. He is currently working at POSTECH as a research assistant professor. He has studied the electronic struc-

tures of a wide variety of solid state materials on the basis of first principles density functional theory calculations.

^aKey Laboratory of Computational Physical Sciences (Ministry of Education), State Key Laboratory of Surface Physics, and Department of Physics, Fudan University, Shanghai 200433, P.R. China

^bDepartment of Chemistry, North Carolina State University, Raleigh, North Carolina 27695-8204, USA. E-mail: hxiang@fudan.edu.cn, mike_whangbo@ncsu.edu

^cDepartment of Chemistry and Research Institute for Basic Sciences, Kyung Hee University, Seoul 130-701, Korea

> as perturbation, that the DM exchange between adjacent spin sites can become comparable in strength to the Heisenberg spin exchange when the two spin sites are not chemically equivalent, and that the DM interaction between rare-earth and transition-metal cations is governed largely by the magnetic orbitals of the rare-earth cation.

1. Introduction

Compared with strong orbital interactions leading to chemical bonding, the interactions between magnetic ions responsible for magnetic properties are extremely weak. Consequently, the magnetic states are closely packed in energy as depicted in Scheme 1, which makes it impossible to understand the magnetic properties of a system by focusing on a few individual magnetic energy levels. This is in sharp contrast to the case of strong orbital interactions in which the structure and reactivity of a compound can be reasonably well accounted for in terms of its frontier orbitals. What one needs in understanding the magnetic properties of a system is its magnetic excitation energy spectrum, which is described by using a spin Hamiltonian defined in terms of a few spin exchange parameters. The geometrical pattern of the spin exchange paths (or magnetic bonds) is known as the spin lattice. The utility of such a model Hamiltonian is to capture the essence of the underlying physics and chemistry behind the observed magnetic properties by using a spin lattice defined with a minimal set of magnetic bonds. A general spin Hamiltonian describing the magnetic properties of a material with localized electrons can be expressed as

$$\hat{H}_{\text{spin}} = \sum_{i < j} J_{ij} \hat{S}_i \cdot \hat{S}_j + \sum_{i < j} \vec{D}_{ij} \cdot (\hat{S}_i \times \hat{S}_j) + \sum_i A_i S_{iz}^2 + \sum_{i < j} K_{ij} (\hat{S}_i \cdot \hat{S}_j)^2$$

where the first term represents the symmetric exchange interaction, the second term the antisymmetric exchange



interaction, the third term the single-ion anisotropy, and the last term the biquadratic interaction. The symmetric exchange interaction is usually known as the Heisenberg exchange interaction, and the antisymmetric exchange interaction as the DM interaction. Both the DM interaction and the single-ion anisotropy are a consequence of spin-orbit coupling. The biquadratic interaction can be derived by applying the fourth-order perturbation to the Hubbard model. It should be noted that, in capturing the essence of the observed magnetic properties of a magnetic system, a spin Hamiltonian does not require the presence of all the four terms.

The orbital interaction picture familiar to chemists plays a decisive role in understanding the spin lattice that specifies the spin Hamiltonian for a given magnetic system. An important difference between strong and weak orbital interactions should be emphasized. In general, the transition-metal cations, M^{x+} (x = oxidation state), of a magnetic system form



Hyun-Joo Koo

Hyun-Joo Koo studied chemistry at The Catholic University of Korea (Songsim Campus) receiving her bachelor's and master's degrees in 1990 and 1992, respectively. She obtained her PhD in physical chemistry from Sungkyunkwan University in 1997. She worked on electrical and magnetic properties of lowdimensional solid state materials with Professor M.-H. Whangbo at North Carolina State University from August 1997 to Febru-

ary 2004. Since March 2004, she has been a Professor of Chemistry at Kyung Hee University, Seoul. She continuously works on magnetic properties of solid state materials on the basis of first principles electronic structure calculations.



Xingao Gong

Xingao Gong received his physics degree from Hunan Normal University in 1982 and his PhD from the Institute of Solid State Physics, Chinese Academy of Sciences, in 1993. He joined Fudan University in 2000 and is currently a Xi-De Chair Professor of Physics, and is also Director of the Key Laboratory of Computational Physical Sciences, Ministry of Education. His research is focused on computational studies of the structural and elec-

tronic properties of materials. He is a fellow of the American Physical Society.

Dalton Transactions Perspective

ML_n polyhedra with surrounding main-group elements L (typically, n = 4-6). For the magnetic M^{x+} cation, some d-block levels of the ML_n polyhedron are singly occupied thereby becoming magnetic orbitals, in which the M nd-orbitals are combined out-of-phase with the L np-orbitals. In discussing the strong orbital interactions leading to chemical bonding and structure, our focus is on the "head" parts (i.e., the nd orbital parts) of all the occupied d-block levels. However, in discussing the weak orbital interactions leading to magnetic bonds, we focus on the "tail" parts (i.e., the np orbitals on the ligands) of the magnetic d-block levels (i.e., the singly occupied d-block levels).1

The objectives of this review are to briefly survey important concepts and phenomena that one encounters in reading the current literature on magnetic solids and to discuss how to evaluate the parameters of model Hamiltonians in terms of energy-mapping analysis based on first principles electronic structure calculations. This review is intended for those who possess minimal knowledge of the terminologies and mathematical treatments employed in describing magnetic properties. Thus, our discussion will be on a qualitative level from the perspective of electronic structure. In the following discussion, we will use the orbital and spin angular momenta as classical vectors (\vec{L} and \vec{S} , respectively) as well as quantum mechanical operators (\hat{L} and \hat{S} , respectively).

Magnetic insulating states

A. Electronic structures

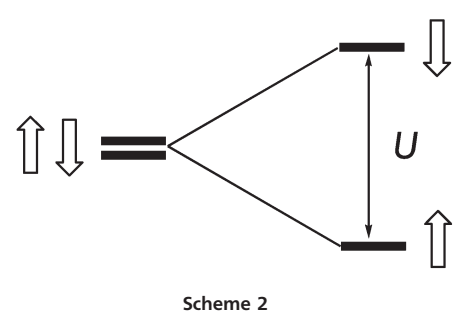
The magnetic properties of a system containing magnetic ions are essentially related to how its electronic energy is affected by an external magnetic field. Since molecules and crystalline solids with magnetic ions are characterized by open-shell electronic structures, it is important to know how such electronic structures are generated. Currently, the electronic structures of



M.-H. Whangbo

M.-H. Whangbo studied chemistry at Seoul National University receiving his bachelor's and master's degrees in 1968 and 1970, respectively. He obtained his PhD in theoretical chemistry from Queen's University in 1974 working with Professors Saul Wolfe and Vedene H. Smith, Jr. After postdoctoral work with Professor Saul Wolfe and then with Professor Roald Hoffmann at Cornell University, he began his academic career in 1978 at

North Carolina State University, where he is a Distinguished Professor of Chemistry. He and his colleagues have explored the structure-property relationships in solid state materials on the basis of electronic structure calculations.



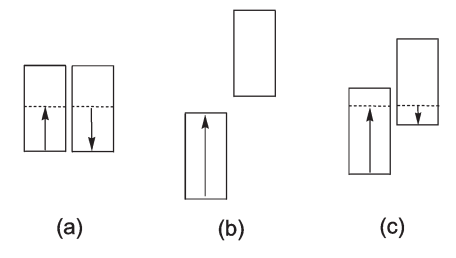


Fig. 1 Filling the up-spin and down-spin bands with two electrons leading to (a) a nonmagnetic metallic, (b) a magnetic insulating and (c) a magnetic metallic

molecules and crystalline solids are described largely on the basis of density functional theory (DFT).2 In the non-spinpolarized DFT, each energy level of a system accommodates two electrons because the up-spin and down-spin levels are treated as degenerate (Scheme 2 (left)). Thus, an energy band of a given solid is described by the up-spin and down-spin subbands that are degenerate in energy. Any solid then with partially filled bands has no energy gap between the highestoccupied and the lowest-unoccupied band levels (Fig. 1a), and is therefore predicted to be a non-magnetic metal. Obviously, this prediction is contrary to the experimental observation that a solid with partially-filled bands can be a magnetic insulator,^{3,4} in which the up-spin and down-spin subbands differ in energy such that an energy gap (i.e., a band gap) occurs between the highest-occupied and the lowest-unoccupied subbands (Fig. 1b).

The failure of the non-spin-polarized DFT in describing magnetic insulators is remedied in part by using spin-polarized DFT, which allows the up-spin and down-spin subbands to differ in their spatial orbitals and hence differ in energy. For most magnetic insulators, this splitting of the up-spin and down-spin subbands given by the spin-polarized DFT is not large enough to produce a band gap (Fig. 1c). This deficiency of the spin-polarized DFT (i.e., the band gap is underestimated) is empirically corrected by using the spin-polarized DFT + U method, in which the effective on-site repulsion U^{eff} = U - J, where U is the on-site repulsion and $J \approx 1$ eV is the on-site exchange-correction, is added on the magnetic ions (mostly transition-metal ions) so as to enhance the spin polarization of their nd orbitals (Scheme 2 (right)). There are two slightly different ways of doing DFT + U calculations. In the DFT + U method of Dudarev et al.5a the energy formula includes only the difference U - J while in the DFT + U

method of Liechtenstein et al. 5b the energy formula includes U and J separately hence allowing greater flexibility in self-consistent-field calculations. For some noncollinear magnetic systems, the magnetocrystalline anisotropy was found to depend strongly on the J parameter.⁶ At the current stage of DFT, it is unfortunately impossible to predict whether a solid with partially filled bands will be a metal or a magnetic insulator. Once such a solid is experimentally known to be a metal or a magnetic insulator, one can carry out spin-polarized DFT + U calculations to determine the range of the U^{eff} values that gives rise to metallic or magnetic insulating states. In describing a magnetic insulator by the DFT + U method, therefore, it is essential to first establish the range of the U^{eff} values producing a band gap and then explore its chemistry and physics on the basis of consistent trends resulting from such Ueff parameters.

The effective on-site repulsion U^{eff} is related to the extent of electron-correlation, which is large for dense electron density distribution. Thus, the value of U^{eff} necessary for DFT + U calculations for nd transition-metal elements should increase as the nd orbital becomes more contracted. The degree of the nd orbital contraction increases in the order 5d < 4d ≪ 3d. This explains why magnetic insulators are much more abundant among compounds of 3d elements than from those of 4d or 5d elements. Nevertheless, magnetic insulators are found from compounds of 4d and 5d elements when they are present in high oxidation states, because their 4d and 5d orbitals become significantly contracted in such a case.

An alternative way of correcting the DFT deficiency of band gap underestimation is the hybrid functional method. 7-9 Here the exchange-correlation functional needed for calculations is obtained by mixing some amount of the Hartree-Fock exchange potential, which overestimates band gap, into the DFT functional. The B3LYP hybrid functional is quite popular in the molecular area. As does the DFT + U method, the hybrid functional method also reduces the self-interaction error of the common DFT functionals. However, there is a key difference. The DFT + U method adds the mean-field Hartree-Focklike term on some specific states (e.g., the nd states of magnetic ions) whereas the hybrid functional method mixes some amount of the exact Hartree-Fock exchange potential to the usual DFT functionals. This means that all states (including the np states of non-magnetic ligands) in the systems are affected by the Hartree-Fock exchange potential in the hybrid functional method. Due to this difference, results of the hybrid functional method may differ from those of the DFT + U method.10

B. Effect of spin arrangement on band gap

In the spin-polarized DFT + U method, the up-spin and downspin nd levels of each spin site are split by U (Scheme 2 (right)). As an example, consider a spin dimer made up of two spin sites 1 and 2 with one orbital and one unpaired spin per site. For the ferromagnetic (FM) arrangement of the two spins (Fig. 2a), both spin sites have the up-spin level lower in energy by U than the down-spin level (by convention). For the AFM

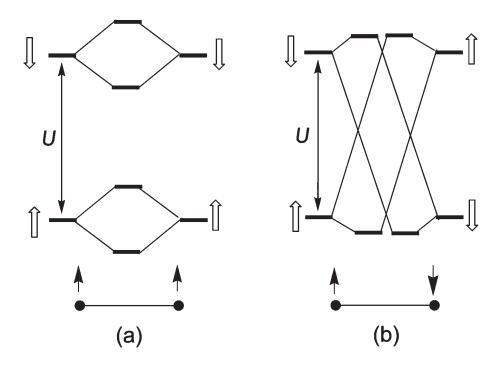


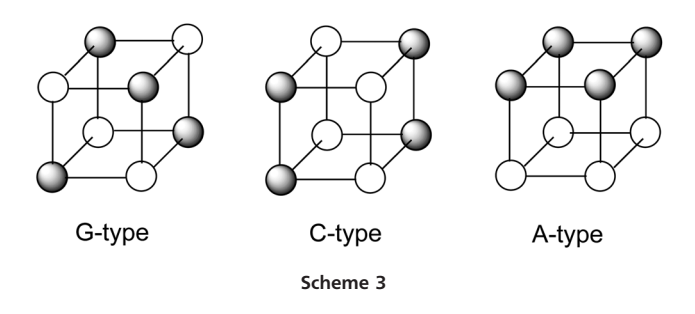
Fig. 2 Dependence of the orbital interactions between two spin sites in a spin dimer on the (a) FM and (b) AFM spin arrangements. Each spin site is assumed to have one electron and one orbital.

arrangement of the two spins (Fig. 2b), the up-spin site has the up-spin level lower in energy by U than the down-spin level, while the opposite is true for the down-spin site. Between the two spin sites, only the levels of the same spin can have orbital interaction so that the interaction between the two spin sites is a degenerate orbital interaction for the FM arrangement, but a nondegenerate orbital interaction for the AFM arrangement. Provided that the electrons at sites 1 and 2 are described by orbitals ϕ_1 and ϕ_2 , respectively, the hopping (resonance) integral t is given by $t = \langle \phi_1 | \hat{H}^{\text{eff}} | \phi_2 \rangle$, where \hat{H}^{eff} is the effective Hamiltonian describing the spin dimer. Then the strength of the orbital interaction between the two spin sites is proportional to the hopping integral t for the FM arrangement, but to t^2/U for the AFM arrangement. In general, t is considerably greater in magnitude than t^2/U .

The above observation has an important implication. Consider a one-dimensional (1D) chain, a two-dimensional (2D) square lattice, and a three-dimensional (3D) cubic lattice made up of equivalent spin sites with one orbital and one electron per site and with the effective hopping integral t between nearest neighbor (NN) sites. In the FM arrangement of the spins, each spin site has the up-spin level lower in energy by U than the down-spin level. Thus, the up-spin and down-spin bands of this FM state, separated by U, will each have the width W = 2zt, where z is the number of NN sites connected by t (i.e., z = 2, 4, 6 for the 1D chain, 2D square and 3D cubic systems, respectively). Therefore, if U > W, the up-spin and down-spin bands are separated with a band gap U-W so that the system will be a magnetic insulator (Fig. 1b). If U < W, however, the up-spin and down-spin bands overlap so that the system becomes a magnetic metal (Fig. 1c). Suppose now that the spins of the 1D, 2D and 3D systems have an AFM arrangement between nearest neighbor sites. Then the widths of the up-spin and down-spin bands are each given by $W = 2zt^2/U$. Since t^2/U is smaller than t in magnitude, so the band width is smaller for the AFM state than for the FM state. Consequently, a system with partially-filled bands is more likely to have a band gap in the AFM state than in the FM state.

A 3D cubic lattice of spin sites may adopt several different AFM states, e.g., the G-, C- and A-types, as depicted in Scheme 3 where the grey and white spheres indicate up- and

Dalton Transactions Perspective



down-spin sites. The G-type structure has AFM interactions in three different directions, the C-type in two different directions, and the A-type in one direction. As a consequence, if all these three AFM states were to have band gaps, their band gaps should decrease in the order G-type > C-type > A-type. Therefore, for an ideal simple cubic 3D magnetic system, it is possible that while the G- and C-type AFM states have a band gap, the A-type AFM state does not, and also that while the G-type AFM state has a band gap, the C- and A-type AFM states do not. Such a dependence of band gap on the type of AFM interactions explains why, as the temperature is lowered, the band gaps of certain antiferromagnets such as NaOsO₃ 11,12 and $\text{Cd}_2\text{Os}_2\text{O}_7$ 13,14 increase continuously without changing their geometries. This kind of metal-insulator transition driven by AFM interactions is known as the Slater transition. 15

3. Magnetic moments and energy levels

A. Magnetization and magnetic susceptibility

The magnetic properties of a compound containing magnetic ions are largely determined by the magnetic moments, $\vec{\mu}$, of the ions. In general, the magnetic moment $\vec{\mu}$ of a system refers to the change of its energy E with respect to the applied magnetic field \vec{H} ,

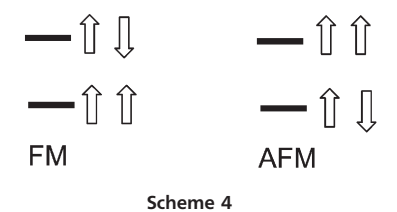
$$\vec{\mu} = -\frac{\partial E}{\partial \vec{H}} \tag{1}$$

A magnetic system is isotropic if its magnetic moment is nonzero in all directions, but is uniaxial if its magnetic moment is nonzero in only one direction. Magnetic ions are characterized by their orbital and spin angular momenta (\vec{L} and \vec{S} , respectively) and hence by the associated magnetic moment $\vec{\mu}$,

$$\vec{\mu} = -(\vec{L} + g\vec{S})\mu_{\rm B},\tag{2}$$

where $\mu_{\rm B}$ is the Bohr magneton, and the electron g-factor, g, is 2.0023 (hereafter, g=2 for simplicity). For magnetic ions in molecules and solids, the orbital momentum is typically quenched ($\vec{L}\approx 0$) due to the low symmetry of their environments so that the magnetic moments are well approximated by the spin-only moments, $\vec{\mu}\approx -2\vec{S}\mu_{\rm B}$.

For a magnetic compound, an experimental quantity of interest at a given temperature is the magnetization \vec{M} , namely, the average moment per unit volume. In general, the



magnetization of a magnetic compound depends on temperature and external magnetic field \vec{H} applied to the compound, because the moments of adjacent magnetic ions tend to have a FM or AFM arrangement due to their spin exchange interactions. For simplicity, consider the energy states of a spin dimer (i.e., a system with two spin sites), although our discussion is also valid for a magnetic system with more than two spin sites. Then the spin exchange interaction generates two states, "magnetic bonding" and "magnetic antibonding" states, as depicted in Scheme 4. These two states represent the "ground state" and "excited state" of the spin dimer, respectively. Any spin exchange path leading to such an interaction may be regarded as a magnetic bond to distinguish from a chemical bond. When the spin exchange interaction is FM, the magnetic bonding and antibonding states have FM and AFM spin arrangements, respectively, but the opposite is the case if the spin exchange interaction is AFM. It is important to recall the very small energy scale involved in magnetic systems. (For example, at the magnetic field of 1 Tesla (H = 1 T), $\mu_B H = 5.8 \times$ 10^{-2} meV = 0.67 K in $k_{\rm B}$ units. Other useful energy scales are 1 meV = 11.6 K = 8.06 cm^{-1} , and 1 cm⁻¹ = 1.44 K.) At a given temperature, the tendency for the moments to adopt a FM or an AFM arrangement is counterbalanced by the available thermal energy k_BT , because both the magnetic bonding and antibonding states will be populated according to the Boltzmann distribution. At high temperature, both states are almost equally populated, so that the magnetization \vec{M} is zero although the magnetic system has nonzero moments locally, thereby leading to the paramagnetic state. As the temperature is lowered, the bonding magnetic state is more preferentially populated than the antibonding magnetic state, hence reducing the paramagnetic behavior.

At a given temperature T the magnetization \vec{M} of a magnetic compound is proportional to the applied magnetic field \vec{H} when the field is weak.

$$\vec{M} = \chi \vec{H},\tag{3}$$

where the proportionality constant is the magnetic susceptibility. At a given magnetic field, the temperature-dependence of the magnetic susceptibility follows the Curie-Weiss law in the high temperature region where the compound is paramagnetic,

$$\chi = \frac{C}{T - \theta} \text{ or } \frac{1}{\chi} = \frac{1}{C}T - \frac{\theta}{C}$$
(4)

where C is the Curie constant (Fig. 3). The $1/\chi$ vs. T plot is linear in the high temperature region where the compound is

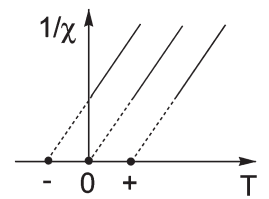


Fig. 3 Plots of $1/\chi$ vs. T showing three different Curie–Weiss temperatures for the cases of $\theta < 0$, $\theta = 0$, and $\theta > 0$. The solid lines indicate that the plots follow the Curie-Weiss law, and the dashed lines that this law is not obeyed in the low temperature region

paramagnetic (solid lines). With decreasing T, the $1/\chi$ vs. T plot usually deviates from linearity. We note that interesting magnetic systems are those whose magnetic susceptibilities deviate strongly from the Curie-Weiss law below a certain temperature because they are likely to exhibit interesting properties due to their strong spin exchange interactions. The two important quantities one can extract from the temperaturedependent magnetic susceptibility by fitting it with the Curie-Weiss law are the effective moment μ_{eff} and the Curie-Weiss temperature, θ . When we use the molar magnetic susceptibility $\chi_{\rm m}$ for a system with spin-S magnetic ions, the effective moment μ_{eff} (in units of μ_{B}) is related to χ_{m} and S as follows,

$$\mu_{\text{eff}} = 2.828 \sqrt{\chi_{\text{m}} T} = 2\sqrt{S(S+1)},$$
 (5)

which provides information about the spin S in the paramagnetic region, and hence about how many unpaired spins the magnetic ion has. On the other hand, the Curie-Weiss temperature θ has information about the nature of the dominant spin exchange interaction. $\theta = 0$, if the spin exchange interactions between magnetic ions are weak so that the magnetic compound is paramagnetic at all temperatures. $\theta < 0$, when the dominant spin exchange interaction is AFM. $\theta > 0$, when the dominant spin exchange interaction is FM. A magnetic compound consisting of spin-S ions can have various spin exchange paths (magnetic bonds) i = 1, 2, ...) and, therefore, have the associated spin exchange constants J_i . In the mean field approximation, 16 the Curie-Weiss temperature θ is related to I_i as

$$\theta = \frac{S(S+1)}{3k_{\rm B}} \sum_{i} z_{i} J_{i},\tag{6}$$

where the summation runs over all adjacent neighbors of a given spin site, z_i is the number of adjacent neighbors connected by J_i .

B. Experimental investigation of magnetic energy levels

Magnetic systems possess low-lying magnetic excited states (Scheme 1) that can be thermally populated according to the Boltzmann distribution. These states are closely packed in energy so that the physical properties of a magnetic system at a given T do not represent the property of a single state but a weighted average of the properties of many magnetic states weighted by their Boltzmann factors. It is the temperaturedependence of this Boltzmann-averaging that governs the magnetic susceptibility (χ) at a given magnetic field \vec{H} or the magnetic specific heat $(C_{p,\text{mag}})$ as a function of temperature. Alternatively, the population changes in the magnetic energy levels can be probed by measuring the magnetization \vec{M} at a very low temperature as a function of magnetic field \vec{H} because the energy $\mu_B H$ supplied to the system changes the populations of its magnetic energy levels.

As discussed above, the magnetic susceptibility, specific heat and magnetization $(\chi, C_{p,mag})$ and \vec{M} , respectively) measurements probe the magnetic excited states indirectly because they represent the properties resulting from various excited states populated according to the Boltzmann distribution. One can probe the individual low-lying magnetic excited states by performing inelastic neutron scattering measurements at a very low temperature where the populations of the magnetic and vibrational excited states are practically zero. In these experiments, a magnetic system is bombarded with a beam of cold (i.e., low-energy) neutrons at a certain energy so that its magnetic excited levels become populated by absorbing energy from the bombarding neutrons. The magnetic excitation energies are deduced by measuring the energy loss of the neutrons scattered away from the compound. The spin-wave dispersion relation (i.e., the dependence of the absorption energy on momentum transfer Q) resulting from these measurements¹⁷ can be analyzed by using various spin Hamiltonians to determine the spin lattice appropriate for the system under investigation.

Mapping analysis for Heisenberg spin exchange

A. Use of eigenstates for an isolated spin dimer^{1,18}

For a half-filled band system with large U, the ground state of the Hubbard Hamiltonian¹⁹ is given (to second order in perturbation theory) by the ground state of the antiferromagnetic Heisenberg Hamiltonian. 19,20 To gain insight into the meaning of the symmetric (or Heisenberg) spin exchange interaction, we consider a spin dimer consisting of two equivalent spin-1/2 spin sites, 1 and 2, with one electron at each spin site (Scheme 5). The energy of the spin dimer arising from the spin exchange interaction between the spins \vec{S}_1 and \vec{S}_2 is given by the Heisenberg spin Hamiltonian

$$\hat{H}_{\text{spin}} = J\hat{S}_1 \cdot \hat{S}_2,\tag{7}$$

where J is the Heisenberg (or symmetric) spin exchange parameter. Note the absence of the negative sign in this expression. With this definition, the AFM and FM spin exchange



Dalton Transactions Perspective

interactions are given by J > 0 and J < 0, respectively. This Hamiltonian describes an isotropic magnetic system because the energy has three Cartesian components due to $\vec{S}_1 \cdot \vec{S}_2 = S_{1x}S_{2x} + S_{1y}S_{2y} + S_{1z}S_{2z}$. Given the dot product between \vec{S}_1 and \vec{S}_2 , the lowest energy for J > 0 occurs when the angle θ between the two spins is 180° (i.e., the spins are AFM), but that for J < 0 when $\theta = 0^{\circ}$ (*i.e.*, the spins are FM). In either case, the Heisenberg spin Hamiltonian leads to a collinear spin arrangement.

In principle, the spin at site i (= 1, 2) of the spin dimer can have either an up-spin α or a down-spin β state. For a single spin S = 1/2 and $S_z = \pm 1/2$ so that, in terms of the $|S, S_z\rangle$ notations, these states are given by $\alpha = |\frac{1}{2}, \frac{1}{2}\rangle$ and $\beta = |\frac{1}{2}, -\frac{1}{2}\rangle$. The states obey the following relationships:

$$\hat{S}_{z}|S, S_{z}\rangle = S_{z}|S, S_{z}\rangle
\hat{S}_{+}|S, S_{z}\rangle = \sqrt{S(S+1) - S_{z}(S_{z}+1)}|S, S_{z}+1\rangle
\hat{S}_{-}|S, S_{z}\rangle = \sqrt{S(S+1) - S_{z}(S_{z}-1)}|S, S_{z}-1\rangle$$
(8)

where $\hat{S}_{+} = \hat{S}_{x} + i\hat{S}_{y}$ and $\hat{S}_{-} = \hat{S}_{x} - i\hat{S}_{y}$ are the ladder operators. Since $\hat{S}(i) = \hat{t}\hat{S}_x(i) + \hat{j}\hat{S}_y(i) + \hat{k}\hat{S}_z(i)$ (i = 1, 2), eqn (7) is rewritten as

$$\hat{H}_{\text{spin}} = J[\hat{S}_x(1)\hat{S}_x(2) + \hat{S}_y(1)\hat{S}_y(2) + \hat{S}_z(1)\hat{S}_z(2)] = J\hat{S}_z(1)\hat{S}_z(2) + (J/2)[\hat{S}_+(1)\hat{S}_-(2) + \hat{S}_-(1)\hat{S}_+(2)]$$
(9)

The eigenstates of $\hat{H}_{\rm spin}$ allowed for the spin dimer are the singlet state $|S\rangle$ and the triplet state $|T\rangle$, which are given by $|S\rangle = [\alpha(1)\beta(2) - \beta(1)\alpha(2)]/\sqrt{2}, |T\rangle = \alpha(1)\alpha(2), \beta(1)\beta(2)$ and $[\alpha(1)\beta(2) + \beta(1)\alpha(2)]/\sqrt{2}$. Note that the broken-symmetry (or Néel) states, $\alpha(1)\beta(2)$ and $\beta(1)\alpha(2)$, interact through \hat{H}_{spin} to give the symmetry-adapted states $|S\rangle$ and $|T\rangle$.

We evaluate the energies of $|T\rangle$ and $|S\rangle$, $E_{\text{spin}}(T)$ and $E_{\rm spin}(S)$, respectively, by using eqn (9) to find $E_{\rm spin}(T) = J/4$ and $E_{\rm spin}(S) = -3J/4$. Thus, the energy difference between the two states is given by

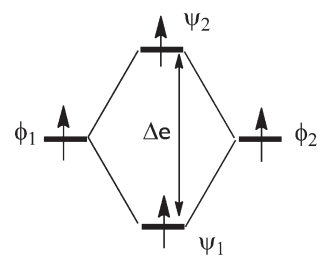
$$\Delta E_{\rm spin} = E_{\rm spin}(T) - E_{\rm spin}(S) = I,\tag{10}$$

so the spin exchange constant J represents the energy difference between the singlet and triplet spin states of the spin dimer. The singlet state is lower in energy than the triplet state if the spin exchange J is AFM (i.e., J > 0), and the opposite is the case if the spin exchange I is FM (i.e., I < 0).

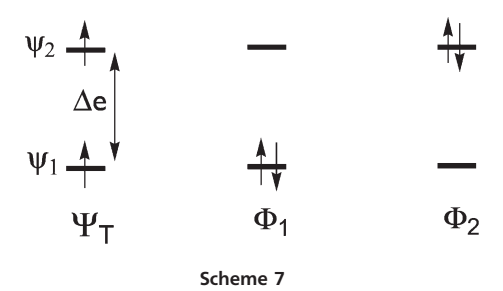
We now examine how the triplet and singlet states of the spin dimer are described in terms of electronic structure calculations. The electronic Hamiltonian $\hat{H}_{\rm elec}$ for this two-electron system can be written as

$$\hat{H}_{\text{elec}} = \hat{h}(1) + \hat{h}(2) + 1/r_{12},$$
 (11)

where $\hat{h}(i)$ (i = 1, 2) is the one-electron energy (*i.e.*, the kinetic and the electron-nuclear attraction energies) of the electron i = 1, 2, and r_{12} is the distance between electrons 1 and 2. Assume that the unpaired electrons at sites 1 and 2 are accommodated in the orbitals ϕ_1 and ϕ_2 , respectively, in the absence of interaction between them. Such singly-occupied orbitals are referred to as magnetic orbitals. The weak interaction between ϕ_1 and ϕ_2 leads to the two levels ψ_1 and ψ_2 of



Scheme 6



the dimer separated by a small energy gap Δe (Scheme 6), which are approximated by $\psi_1 \approx (\phi_1 + \phi_2)/\sqrt{2}$ and $\psi_2 \approx (\phi_1 - \phi_2)/\sqrt{2}$. As depicted in Scheme 7 (left), one of the three triplet-state wave functions is represented by the electron configuration Ψ_T . When Δe is very small (compared with that expected for chemical bonding), the singlet state electron configurations Φ_1 (Scheme 7 (centre)) and Φ_2 (Scheme 7 (right)) are very close in energy, and interact strongly under $\hat{H}_{\rm elec}$ to give $\langle \Phi_1 | \hat{H}_{elec} | \Phi_2 \rangle = K_{12}$, where K_{12} is the exchange repulsion between ϕ_1 and ϕ_2 (see below). Thus the true singlet state Ψ_S is described by the lower-energy state of the configuration-interaction (CI) wave functions Ψ_i (i = 1, 2),

$$\Psi_i = C_{1i}\Phi_1 + C_{2i}\Phi_2 \ (i = 1, 2), \tag{12}$$

namely, $\Psi_S = \Psi_1$. The energies of Ψ_S and Ψ_T , $E_{CI}(S)$ and $E_{CI}(T)$, respectively, can be evaluated in terms of \hat{H}_{elec} by using the dimer orbitals ψ_1 and ψ_2 determined from the calculations for the triplet state Ψ_{T} . Then, after some manipulations, the electronic energy difference between the singlet and triplet state is written as¹⁸

$$\Delta E_{\rm CI} = E_{\rm CI}(S) - E_{\rm CI}(T) = -2K_{12} + \frac{(\Delta e)^2}{U^{\rm eff}}$$
 (13)

where K_{12} is the exchange repulsion $K_{12} = \langle \phi_1(1)\phi_2(2)/1/r_{12}/r_{12}\rangle$ $\phi_2(1)\phi_1(2)$. The effective on-site repulsion U^{eff} is given by U^{eff} = $J_{11} - J_{12}$, where J_{11} and J_{12} are the Coulomb repulsions $J_{11} =$ $\langle \phi_1(1)\phi_1(2)/1/r_{12}/\phi_1(1)\phi_1(2)\rangle$ and $J_{12} = \langle \phi_1(1)\phi_2(2)/1/r_{12}/\phi_1(1)$ $\phi_2(2)$. Therefore, by mapping the energy spectrum of $\hat{H}_{\rm spin}$ onto that of \hat{H}_{elec} , namely, $\Delta E_{spin} = \Delta E_{CI}$, we obtain

$$J = \Delta E_{\rm CI} = -2K_{12} + \frac{(\Delta e)^2}{U^{\rm eff}}$$
 (14)

It is important to note the qualitative aspect of the spin exchange J on the basis of the above expression. Since the

repulsion terms K_{12} and $U^{\rm eff}$ are always positive, the spin exchange J is divided into the FM and AFM components J_F (<0) and J_{AF} (>0), respectively. That is,

$$J = J_{\rm F} + J_{\rm AF},\tag{15}$$

where

$$J_{\rm F} = -2K_{12} \tag{16a}$$

$$J_{\rm AF} = \frac{(\Delta e)^2}{U^{\rm eff}} \tag{16b}$$

The FM term $J_{\rm F}$ becomes stronger with increasing the exchange integral K_{12} , which in turn increases with increasing the overlap density, $\phi_1\phi_2$. The AFM term J_{AF} becomes stronger with increasing Δe , which in turn becomes larger with increasing the overlap integral, $\langle \phi_1 | \phi_2 \rangle$. In addition, the J_{AF} term becomes weaker with increasing the on-site repulsion, U^{eff} .

B. Use of broken-symmetry states for general magnetic solids

For a general magnetic system, it is practically impossible to determine the eigenvalue spectrum of either \hat{H}_{elec} or \hat{H}_{spin} . However, for broken-symmetry states, which are not eigenstates of \hat{H}_{elec} and \hat{H}_{spin} , their relative energies can be readily determined in terms of both \hat{H}_{elec} and \hat{H}_{spin} . With DFT calculations, the energy-mapping for a spin dimer between the energy spectra of \hat{H}_{elec} and \hat{H}_{spin} is carried out by using highspin and broken-symmetry states (|HS) and respectively). 1,21-25 For example, let us reconsider the spin dimer shown in Scheme 5, for which the pure-spin |HS> and |BS> states are given by

$$|HS\rangle = \alpha(1)\alpha(2) \text{ or } \beta(1)\beta(2)$$

 $|BS\rangle = \alpha(1)\beta(2) \text{ or } \beta(1)\alpha(2)$ (17)

Here the |HS| state is an eigenstate of the spin Hamiltonian $\hat{H}_{\rm spin}$ in eqn (7), but the |BS\rangle state is not. In terms of this Hamiltonian, the energies of the collinear-spin states |HS> and $|BS\rangle$, $E_{spin}(HS) = \langle HS | \hat{H}_{spin} | HS \rangle$ and $E_{spin}(BS) = \langle BS | \hat{H}_{spin} | BS \rangle$, respectively, are given by $E_{\rm spin}({\rm HS}) = J/4$ and $E_{\rm spin}({\rm BS}) = -J/4$. Thus,

$$\Delta E_{\text{spin}} = E_{\text{spin}}(\text{HS}) - E_{\text{spin}}(\text{BS}) = J/2. \tag{18}$$

In terms of DFT, the electronic structures of the |HS> and |BS| states are readily calculated to determine their energies, $E_{\rm DFT}({\rm HS})$ and $E_{\rm DFT}({\rm HS})$, respectively, and hence obtain the energy difference

$$\Delta E_{\rm DFT} = E_{\rm DFT}({\rm HS}) - E_{\rm DFT}({\rm BS}). \tag{19}$$

Consequently, by mapping $\Delta E_{\rm spin}$ onto $\Delta E_{\rm DFT}$, we obtain

$$J/2 = \Delta E_{\rm DFT}.\tag{20}$$

The energy-mapping analysis based on DFT calculations employs the broken-symmetry state that is not an eigenstate of the spin Hamiltonian (eqn (7)). For a general spin Hamiltonian defined in terms of several spin exchange parameters, it is impossible to determine its eigenstates analytically in

terms of spin exchange parameters to be determined and it is also difficult to determine them numerically even when their values are known. For any realistic magnetic system requiring a spin Hamiltonian defined in terms of various spin exchange parameters, the energy-mapping analysis based on DFT greatly facilitates the quantitative evaluation of the spin exchange parameters because it does not rely on the eigenstates but on the broken-symmetry states of the spin Hamiltonian. For broken-symmetry states, the energy expressions of the spin Hamiltonian can be readily written down (see below) and the corresponding electronic energies can be readily determined by DFT calculations as well.

In general, the magnetic energy levels of a magnetic system are described by employing a Heisenberg spin Hamiltonian $\hat{H}_{\rm spin}$ defined in terms of several different spin exchange parameters,

$$\hat{H}_{\rm spin} = \sum_{i > i} J_{ij} \hat{S}_i \cdot \hat{S}_j \tag{21}$$

where \hat{S}_i and \hat{S}_i are the spins at the spin sites i and j, respectively, and J_{ii} are the spin exchange parameters describing the sign and strength of the interaction between the spin sites i and j. This model Hamiltonian generates a set of magnetic energy levels as the sum of pairwise interactions $J_{ii}\hat{S}_{i}$: \hat{S}_{i} . It is interesting that the summation of such "two-body interactions" can reasonably well describe the magnetic energy spectrum. This is due to the fact that spin exchange interactions are determined primarily by the tails of magnetic orbitals (see Section 5). The spin exchange constants J_{ii} of a given magnetic system can be evaluated by employing the energymapping method described below. (Heisenberg spin exchange constants can also be evaluated by using the four-state energymapping method.²³ See Appendix.)

- (a) Select a set of N spin exchange paths J_{ij} (= $J_1, J_2, ..., J_N$) for a given magnetic system on the basis of inspecting the geometrical arrangement of its magnetic ions and also considering the nature of its M-L-M superexchange and M-L···L-M super-superexchange paths.
- (b) Construct N + 1 ordered spin states (i.e., broken-symmetry states) i = 1, 2, ..., N + 1, in which all spins are collinear so that any given pair of spins has either a FM or AFM arrangement. For a general spin dimer whose spin sites i and j possess N_i and N_i unpaired spins (hence, spins $S_i = N_i/2$ and $S_i = N_i/2$), respectively, the spin exchange energies of the FM and AFM arrangements ($E_{\rm FM}$ and $E_{\rm AFM}$, respectively) are given by²⁴

$$E_{\rm FM} = +N_i N_i J_{ij}/4 = +S_i S_i J_{ij},$$

$$E_{AFM} = -N_i N_i J_{ii} / 4 = -S_i S_i J_{ii},$$
 (22)

where J_{ij} (= J_1 , J_2 , ..., J_N) is the spin exchange parameter for the spin exchange path ij = 1, 2, ..., N. Thus, the total spin exchange energy of an ordered spin arrangement is readily obtained by summing up all pairwise interactions to find the energy expression $E_{\text{spin}}(i)$ (i = 1, 2, ..., N + 1) in terms of the parameters to be determined and hence the N relative energies

$$\Delta E_{\text{spin}}(i-1) = E_{\text{spin}}(i) - E_{\text{spin}}(1) \ (i=2,3, ..., N+1)$$
 (23)

Dalton Transactions Perspective

(c) Determine the electronic energies $E_{DFT}(i)$ of N+1ordered spin states i = 1, 2, ..., N + 1 by DFT calculations to obtain the N relative energies

$$\Delta E_{\text{DFT}} (i-1) = E_{\text{DFT}}(i) - E_{\text{DFT}}(1) (i=2,3, ..., N+1)$$
 (24)

As already mentioned, DFT calculations for a magnetic insulator tend to give a metallic electronic structure because the electron correlation of a magnetic ion leading to spin polarization is not well described. Since we deal with the energy spectrum of a magnetic insulator, it is necessary that the electronic structure of each ordered spin state obtained from DFT calculations be magnetic insulating. To ensure this aspect, it is necessary to perform DFT + U calculations⁵ by adding on-site repulsion U^{eff} on magnetic ions. Furthermore, as can be seen from eqn (16b), the AFM component of a spin exchange decreases with increasing U^{eff} so that the magnitude and sign of a spin exchange constant may be affected by U^{eff} . It is therefore necessary to carry out DFT + U calculations with several different U^{eff} values.

(d) Finally, determine the values of $J_1, J_2, ..., J_N$ by mapping the N relative energies ΔE_{DFT} onto the N relative energies $\Delta E_{
m spin}$,

$$\Delta E_{\text{DFT}} (i-1) = \Delta E_{\text{spin}} (i-1) (i=2,3, ..., N+1)$$
 (25)

In determining N spin exchanges J_1 , J_2 , ..., J_N , one may employ more than N + 1 ordered spin states, hence obtaining more than N relative energies ΔE_{DFT} and ΔE_{spin} for the mapping. In this case, the N parameters $J_1, J_2, ..., J_N$ can be determined by performing least-squares fitting analysis.

It is well-known that common DFT functionals suffer from the self-interaction error, i.e., a single electron interacts with itself, which is unphysical. This error results in a spurious delocalization of orbitals including magnetic orbitals. As a consequence, spin exchange interactions are overestimated by the usual DFT methods. One way to reduce the self-interaction error is to use the DFT + U method, in which the on-site Coulomb interaction is taken into consideration. This on-site interaction is parameterized by the effective on-site Coulomb interaction U and on-site exchange interaction J. By adding such Hartree-Fock-like terms, the DFT + U method makes the magnetic orbitals more localized and decreases the overlap between magnetic orbitals hence reducing the magnitudes of spin exchange interactions. Currently, there is no reliable way of determining the U and J parameters needed for DFT + U calculations. A promising method²⁶ might be to compare the DFT + U results with those obtained by the hybrid functional method.

Given DFT + U calculations with several different U^{eff} values, one obtains several sets of the $J_1, J_2, ..., J_N$ values. It is important to find trends common to these sets. What matters in finding a spin lattice are the relative magnitudes of the spin exchanges. To determine which set is most appropriate, one might evaluate the Curie-Weiss temperature θ in terms of the calculated $J_1, J_2, ..., J_N$ values (eqn (6)). There is no guarantee, of course, that the set that gives θ closet to the experimental

value represents the best set. As already pointed out, the purpose of using a spin Hamiltonian is to quantitatively describe the observed experimental data (namely, the temperature dependence of χ , $C_{p,\text{mag}}$ and \vec{M} as well as the excitation spectrum measured from neutron scattering measurements) with a minimal set of J_{ij} values hence capturing the essence of the chemistry and physics involved. Experimentally, such a set of J_{ij} values for a given magnetic system is deduced first by choosing a few spin exchange paths J_{ij} that one considers as important for the system and then by evaluating their signs and magnitudes such that the energy spectrum of the resulting spin Hamiltonian best simulates the observed experimental data. The numerical values of J_{ij} deduced from this fitting analysis depend on what spin lattice model one employs for the fitting (see ref. 27 for example), and hence more than one spin lattice may fit the experimental data equally well.

This non-uniqueness of the fitting analysis has been the source of controversies in the literature over the years. From the viewpoint of doing physics (namely, providing a quantitative mathematical analysis using a model Hamiltonian with minimum adjustable parameters) for a given magnetic system, it is appealing to select a spin lattice model that can generate interesting and novel results. If the chosen spin lattice model is not the true spin lattice for the system, then the physics generated is irrelevant for the system and becomes "a solution in search of a problem". The latter situation occurs not infrequently in the field of condensed matter magnetic studies. Ultimately, the spin lattice of a magnetic system deduced from experimental fitting analysis should be consistent with the one determined from the energy-mapping analysis based on DFT calculations, because the observed magnetic properties are a consequence of the electronic structure of the magnetic system.

Qualitative aspects of Heisenberg spin exchange

Given a magnetic solid made up of ML_n polyhedra containing a magnetic transition cation M^{x+} (x = oxidation state), there may occur two types of spin exchange paths, namely, M-L-M superexchange and/or M-L···L-M super-superexchange paths. The factors governing the signs and magnitudes of M-L-M superexchanges have been well established more than six decades ago. 28,29 However, the importance of M-L···L-M super-superexchange paths has been realized not long ago. In leading to AFM interactions, M-L...L-M super-superexchanges can be much stronger than M-L-M superexchanges. What was not realized in the early studies of M-L-M superexchanges is the importance of magnetic orbitals of Mx+ cations, in which the M nd-orbitals are combined out-of-phase with the L nporbitals. In M-L···L-M spin exchanges the magnetic orbitals of the two metal sites can interact strongly as long as their L nporbital tails can interact through the L...L contact. In this section we examine qualitatively the through-space and

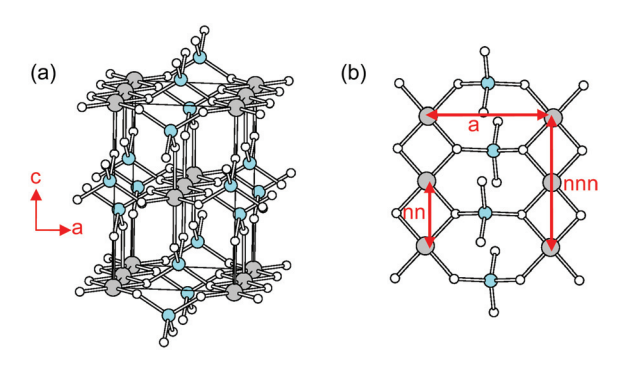


Fig. 4 (a) Perspective view of the crystal structure of LiCuVO₄ showing the CuO_2 ribbon chains interconnected by VO_4 tetrahedra. The Cu atoms are indicated by large grey circles, the V atoms by cyan circles, and the O atoms by small unshaded circles. (b) The intrachain spin exchange paths J_{nn} and J_{nnn} as well as the interchain spin exchange path J_a of LiCuVO₄.

through-bond orbital interactions that govern $M-L\cdots L-M$ super-superexchanges.

As a representative example capturing the essence of spin exchange interactions, let us examine those of $LiCuVO_4^{30-32}$ in which the CuO_2 ribbon chains, made up of edge-sharing CuO_4 square planes running along the b-direction, are interconnected along the a-direction by sharing corners with VO_4 tetrahedra. This is shown in Fig. 4a. In $LiCuVO_4$ the Cu^{2+} (S=1/2, d^9) ions are magnetic, but the V^{5+} (d^0) ions are nonmagnetic. As for the spin exchange paths of $LiCuVO_4$, we consider the nearest neighbor (NN) and next-nearest-neighbor (NNN) intrachain spin exchanges, J_{nn} and J_{nnn} , respectively, in each CuO_2 ribbon chain as well as the interchain spin exchange J_a along the a-direction (Fig. 4b).

The magnetic orbital of the Cu^{2+} ($S = 1/2, d^9$) ion is given by the $x^2 - y^2$ σ^* -antibonding orbital contained in the CuO₄ square plane (Fig. 5a), in which the Cu 3d $x^2 - y^2$ orbital is combined out-of-phase with the 2p orbitals of the four surrounding O ligands. As already emphasized, 1 it is not the "head" part (the Cu 3d $x^2 - y^2$ orbital) but the "tail" part (the O 2p orbitals) of the magnetic orbital that controls the magnitudes and signs of these spin exchange interactions. Let us first consider the Cu-O-Cu superexchange J_{nn} . When the $x^2 - y^2$ magnetic orbitals ϕ_1 and ϕ_2 of the two spin sites are brought together to form the Cu-O-Cu bridges, the O 2p orbital tails at the bridging O atoms make a nearly orthogonal arrangement (Fig. 5b). Thus, the overlap integral $\langle \phi_1/\phi_2 \rangle$ between the two magnetic orbitals is almost zero, which leads to $J_{\rm AF} \approx 0$. In contrast, the overlap density $\phi_1\phi_2$ of the magnetic orbitals is substantial, which leads to nonzero $J_{\rm F}$. As a consequence, the $J_{\rm nn}$ exchange becomes FM. 31,32

For the intra-chain Cu–O···O–Cu super-superexchange $J_{\rm nnn}$ (Fig. 5c), the O 2p orbital tails of the magnetic orbitals ϕ_1 and ϕ_2 at the terminal O atoms are well separated by the O···O contacts. Thus, the overlap density $\phi_1\phi_2$ of the magnetic orbitals is negligible leading to $J_{\rm F}\approx 0$. However, the overlap integral $\langle \phi_1|\phi_2\rangle$ is nonzero because the O 2p tails of ϕ_1 and ϕ_2 overlap through the O···O contacts. This through-space interaction between ϕ_1 and ϕ_2 produces a large energy split Δe between ψ_+

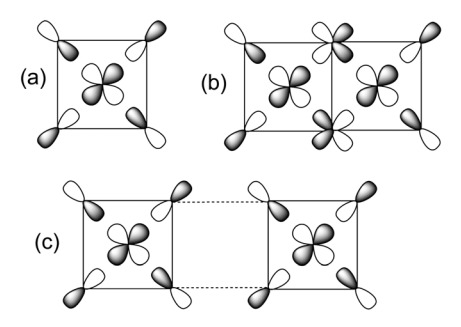


Fig. 5 (a) The $x^2 - y^2$ magnetic orbital of a CuO₄ square plane. (b) The Cu–O–Cu spin exchange interaction between nearest-neighbor CuO₄ square planes in a CuO₂ ribbon chain. (c) The Cu–O···O–Cu spin exchange interaction between next-nearest neighbor CuO₄ square planes in a CuO₂ ribbon chain.

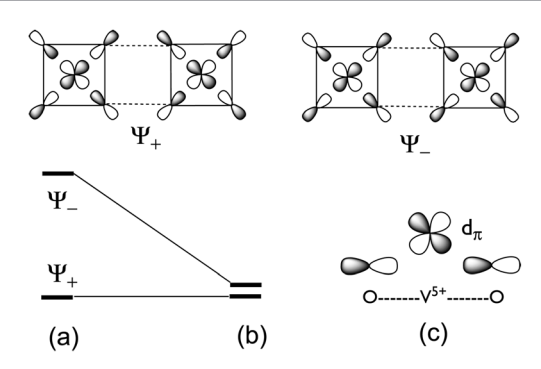


Fig. 6 The through-space and through-bond interactions between the two x^2-y^2 magnetic orbitals in the Cu–O···V⁵⁺····O–Cu interchain spin exchange J_a in LiCuVO₄. (a) The energy split between ψ_+ and ψ_- due to the through-space interaction. (b) The energy split between ψ_+ and ψ_- due to the through-space and through-bond interactions. (c) The bonding interaction of the V d_{π} orbital with the O 2p tails of ψ_- in the O···V⁵⁺···O bridge.

and ψ_- , which are in-phase and out-of-phase combinations of ϕ_1 and ϕ_2 , respectively (Fig. 6a), thereby leading to nonzero $J_{\rm AF}$. Consequently, the $J_{\rm nnn}$ exchange becomes AFM. 31,32

In the interchain spin exchange path J_a , the two CuO₄ square planes are corner-shared with VO4 tetrahedra. In the Cu-O···V⁵⁺···O-Cu super-superexchange paths, the empty V 3d orbitals should interact in a bonding manner with the Cu $x^2 - y^2$ orbitals. In the absence of the V 3d orbitals, the energy split Δe between ψ_+ and ψ_- arising from the through-space interaction between ϕ_1 and ϕ_2 would be substantial, as expected from the intrachain exchange J_{nnn} , so that one might expect a strong AFM exchange for J_{inter} . However, in the Cu-O···V⁵⁺····O-Cu exchange paths, the bridging VO₄ units provide a throughbond interaction between the empty V $3d_{\pi}$ orbitals and the O 2p tails of the magnetic orbitals on the O···O contacts. By symmetry, this through-bond interaction is possible only with ψ_{-} (Fig. 6b,c). The V $3d_{\pi}$ orbital being empty, the O 2p tails of ψ_{-} on the O···O contacts interact in-phase with the empty V $3d_{\pi}$ orbital hence lowering the ψ_{-} level, whereas ψ_{+} is unaffected by the V $3d_{\pi}$ orbital, thereby reducing the energy split Δe between ψ_{+} and ψ_{-} of the Cu-O···V⁵⁺····O-Cu exchange paths and consequently weakening the interchain spin exchange J_a . ^{31,32} As a consequence, the magnetic properties are dominated by the 1D character of the CuO₂ ribbon chain $via J_{nn}$ and J_{nnn} .

(a) (b) Ψ_{+} Ψ_{-} (c) Ψ_{-} Ψ_{-}

Dalton Transactions

Fig. 7 The through-space (TS) and through-bond (TB) interactions between the two x^2-y^2 magnetic orbitals in the Cu–O····V⁵⁺····O–Cu spin exchange found in BaCu₂V₂O₈. (a) The spin dimer in which two CuO₄ square planes stacked on top of each other are bridged by two VO₄ tetrahedra. The Cu atoms are indicated by large grey circles, the V atoms by cyan circles, and the O atoms by small unshaded circles. (b) The energy split between ψ_+ and ψ_- due to the TS interaction, and that due to the TS and TB interactions. (c) The bonding interactions of the V d orbitals with the O 2p tails of ψ_- in the O····V⁵⁺···O bridges.

As another example of showing the interplay between the through-space and through-bond spin exchange interaction, we consider the spin gap system BaCu₂V₂O₈ ³³⁻³⁵ in which two CuO₄ square planes, stacked on top of each other, are bridged by two VO₄ tetrahedra as illustrated in Fig. 7a. Since the two CuO₄ units are nearly parallel to each other, the overlap between ϕ_1 and ϕ_2 is of δ -type so that the through-space interaction between ϕ_1 and ϕ_2 leads to a negligibly small energy split Δe between ψ_+ and ψ_- (Fig. 7b). In the Cu–O···V⁵⁺····O–Cu exchange paths, the bridging VO₄ units provide a throughbond interaction between the empty V 3d orbitals and the O 2p tails on the O···O contacts. This through-bond interaction is possible only with ψ_{-} (Fig. 7c) in which the O 2p tails of the O···O contacts are out-of-phase. These O 2p tails interact inphase with the empty V 3d orbital hence lowering the ψ_{-} level below ψ_+ , while ψ_+ is unaffected by the V $3d_\pi$ orbital. This enhances the energy split Δe between ψ_+ and ψ_- of the Cu-O···V⁵⁺···O-Cu exchange paths and hence leads to a strong AFM spin exchange (Fig. 7b), 35 which is responsible for the observed spin gap behavior of BaCu₂V₂O₈ 33 and also for the observation from the 51V NMR study34 that the V sites have nonzero spin densities. The latter reflects the fact that the V 3d orbitals mix into the magnetic orbital ψ_{-} .

When these ML_n polyhedra containing M^{x^+} cations are condensed together by sharing a corner, an edge or a face, they give rise to M–L–M superexchanges described by the Goodenough–Kanamori rules. When these polyhedra are not condensed by sharing corners, they give rise to M–L···L–M supersuperexchanges. It is the L np tails of the magnetic orbitals that control the magnitudes and signs of such spin exchange interactions. Concerning the M–L···L–M spin exchanges, there are several important consequences of this observation:

- (a) The strength of a given M-L···L-M spin exchange is not determined by the shortness of the M···M distance, but rather by that of the L···L distance; it is strong when the L···L distance is in the vicinity of the van der Waals radii sum or shorter.¹
- (b) In a given magnetic system consisting of both M–L–M and M–L···L–M spin exchanges, the M–L···L–M spin exchanges are very often stronger than the M–L–M spin exchanges.

(c) The strength of an M–L···L–M spin exchange determined by through-space interaction between the L np tails on the L···L contact can be significantly modified when the L···L contact has a through-bond interaction with the intervening d^0 metal cation A^{y+} (y= oxidation state) 31,35 or even the p^0 metal cation (e.g., Cs^+ as found for Cs_2CuCl_4 36). Such an M–L··· A^{y+} ····L–M spin exchange becomes strong if the corresponding M–L···L–M through-space exchange is weak, but becomes weaker if the corresponding M–L···L–M through-space exchange is strong. This is so because the empty d_π orbital of A^{y+} interacts only with the ψ_- orbital of the M–L···L–M exchange. In general, the empty d_π orbital has a much stronger through-bond effect than does the empty p_π orbital.

6. Magnetic structure

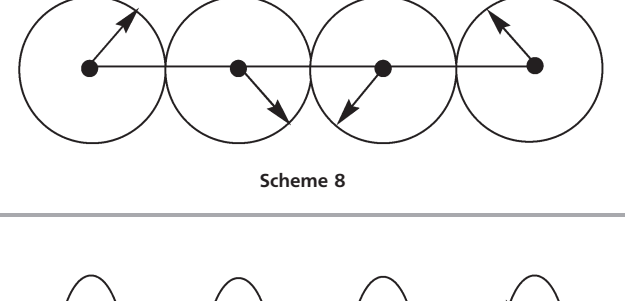
The presence of various spin exchange interactions in crystalline solids gives rise to a variety of spin arrangements and magnetic properties. In this section, we will briefly describe typical magnetic phenomena realized in crystalline solids and their causes from the viewpoint of electronic/magnetic structures.

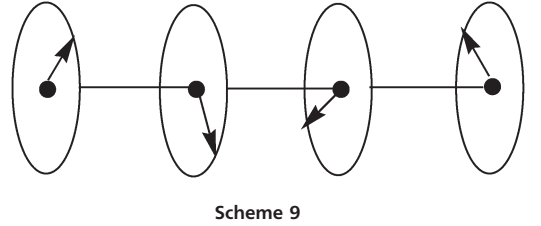
A. Spin frustration and non-collinear spin arrangement

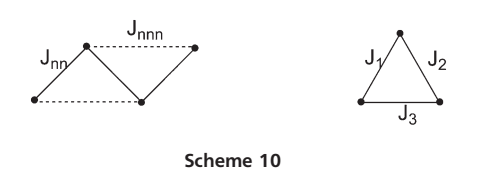
In each ${\rm CuO_2}$ ribbon chain of ${\rm LiCuVO_4}$ discussed in the previous section, a FM arrangement of all spins would be energetically favorable if only the FM exchange $J_{\rm nn}$ is considered. However, this arrangement is energetically unfavorable according to the AFM exchange $J_{\rm nnn}$ because it forces an AFM arrangement for every NNN spin pair. Consequently, the spin exchanges $J_{\rm nn}$ and $J_{\rm nnn}$ in each ${\rm CuO_2}$ ribbon chain give rise to spin frustration. 37,38 To reduce the extent of this spin frustration, which arises from a collinear spin arrangement, and hence lower the energy, each ${\rm CuO_2}$ ribbon chain adopts a spiral spin arrangement 30 in which the NN spin pairs are nearly orthogonal to each other while the NNN spin pairs have an AFM arrangement. In reciprocal units the periodicity q of the spiral spin arrangement is related to the $J_{\rm nn}/J_{\rm nnn}$ ratio as 31,39

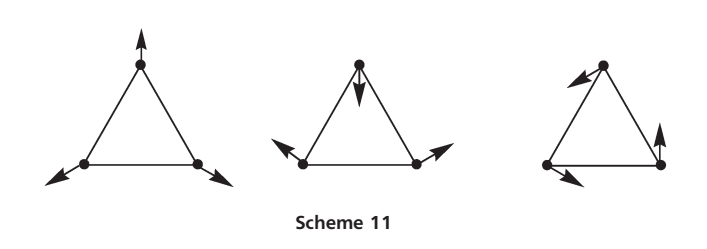
$$q = \frac{1}{2\pi} \arctan\left(-\frac{J_{\rm nn}}{4J_{\rm nnn}}\right). \tag{26}$$

For example, when $J_{\rm nn}=0$ and $J_{\rm nnn}>0$, q=0.25 so that the magnetic unit cell quadruples along the chain direction. In principle, such a spiral-spin arrangement can be cycloidal (Scheme 8) in which the plane of the spin rotation contains the chain-propagation direction, or helical (Scheme 9) in which the plane of the spin rotation is perpendicular to the chain-propagation direction. It is very important to note that Heisenberg spin exchange interactions determine the relative spin arrangement of a magnetic system, but do not control the absolute spin orientation in space. It is ${\rm SOC}^{40}$ and magnetic dipole–dipole (MDD) interactions⁴¹ that provide the preferred spin orientation in space.

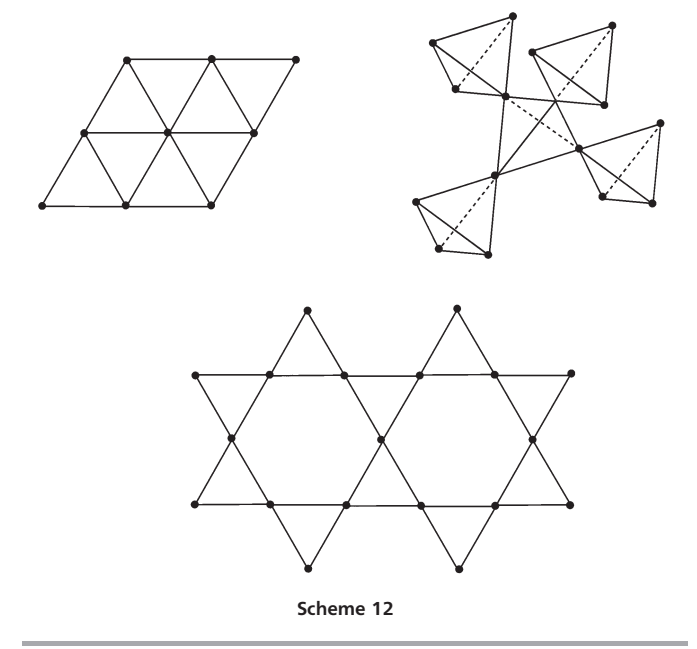








The spin frustration in the linear CuO2 ribbon chain arising from J_{nn} and J_{nnn} is topologically equivalent to that in a zigzag chain with J_{nn} and J_{nnn} (Scheme 10 (left)), which consists of $(J_{nn}, J_{nn}, J_{nnn})$ triangles. In general, any spin exchange triangle (J_1, J_2, J_3) made up of three magnetic bonds (Scheme 10 (right)) is spin-frustrated if all magnetic bonds are AFM or if two magnetic bonds are FM and the remaining one is AFM. A spin-frustrated equilateral triangle made up of an AFM exchange J ($J_1 = J_2 = J_3 = J > 0$) adopts the 120° spin arrangements (i.e., non-collinear spin arrangements) (Scheme 11). Representative examples of extended solids showing spin frustration are the triangular (Scheme 12 (top left)), Kagome (Scheme 12 (bottom)) and pyrochlore (Scheme 12 (top right)) spin lattices with NN AFM spin exchange. From the viewpoint of energy, the presence of spin frustration means that the magnetic ground state is highly degenerate, namely, many different spin arrangements have the same energy. How this degeneracy can be broken by weak perturbation is a fascinating research topic in condensed matter physics. Experimentally, a magnetic system with dominant AFM interaction (i.e., with negative Curie-Weiss



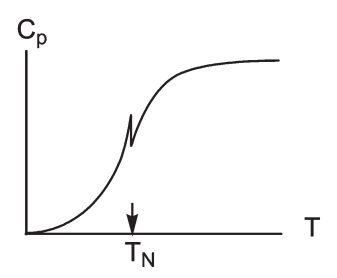


Fig. 8 The temperature dependence of the specific heat of a magnetic solid undergoing a 3D AFM ordering below T_{N} .

temperature θ) is considered to be significantly spin-frustrated if the frustration index37

$$f = |\theta|/T_{\rm N} \tag{27}$$

is greater than 6, where T_N is the Néel temperature, namely, the temperature below which the system undergoes a 3D AFM ordering.

B. Long-range antiferromagnetic order

A magnetic system described by a Heisenberg spin Hamiltonian undergoes a 3D long-range magnetic order if interactions between spin sites occur in all three directions and if there is no strong spin frustration, so that its magnetic properties are 3D in nature.42 Here, the interactions leading to a long-range magnetic order can be spin exchange interactions and/or MDD interactions (see below). The unambiguous proof for the occurrence of a 3D AFM order is given by a λ -anomaly in the temperature dependence of the specific heat $C_{p,tot}$ (Fig. 8), which has contributions from the populated vibrational and magnetic energy levels. Thus, magnetic specific heat $C_{p,mag}$ is obtained from the measured $C_{p,tot}$ by subtracting the vibrational (phonon) specific heat $C_{p,vib}$, *i.e.*,

 $C_{
m p,mag} = C_{
m p,tot} - C_{
m p,vib}$, but the determination of $C_{
m p,vib}$ is a nontrivial task. For a magnetic solid made up of spin-S magnetic ions, the magnetic entropy change ΔS associated with a 3D magnetic ordering is related to the loss of the spin degrees of freedom, 2S+1, as

Dalton Transactions

$$\Delta S = R \ln(2S + 1) \tag{28}$$

Experimentally, ΔS is determined from the measured $C_{\rm p}$, $_{\rm mag}$ νs . T data as

$$\Delta S = \int \frac{C_{\text{p,mag}}}{T} dT \tag{29}$$

It should be pointed out that the ΔS value expected from eqn (29) assumes that there is no short-range order before the 3D long-range order takes place (see below).

In most cases of magnetic solids undergoing a 3D AFM order, spin exchange interactions occur in three directions. However, a 2D AFM system can undergo a 3D AFM order at high T_N with the help of MDD interactions, as found for the two-leg spin ladder compound Sr₃Fe₂O₅. 41,43,44 In this compound FeO₄ square planes containing high-spin Fe²⁺ (S = 2, d⁶) ions share corners to form Fe₂O₅ two-leg spin ladders along the b-direction, which are stacked along the a-direction to form Fe₂O₅ slabs parallel to the *ab*-plane (Fig. 9a and b). These slabs repeat along the c-direction such that adjacent Fe₂O₅ slabs differ in their a-axis height by a/2 and in their b-axis height by b/2. The high-spin Fe^{2+} (d⁶) ion of an FeO_4 square plane has the d-state split pattern $z^2 < (xz,yz) < xy < x^2 - y^2$ (Fig. 10a),⁴¹ and hence the electron configuration $(z^2)^2(xz,$ $yz)^{1}(xy)^{1}(x^{2}-y^{2})^{1}$ leading to four magnetic orbitals. Within each two-leg spin ladder, the spin exchanges $J_{||}$ along the legs and J_{\perp} along the rungs are both strongly AFM due to their linear Fe-O-Fe exchange paths and the $x^2 - y^2$ magnetic orbitals involved (Fig. 9b). The spin exchange J_a along the stacking direction of the spin ladders is also strongly AFM (Fig. 9d)

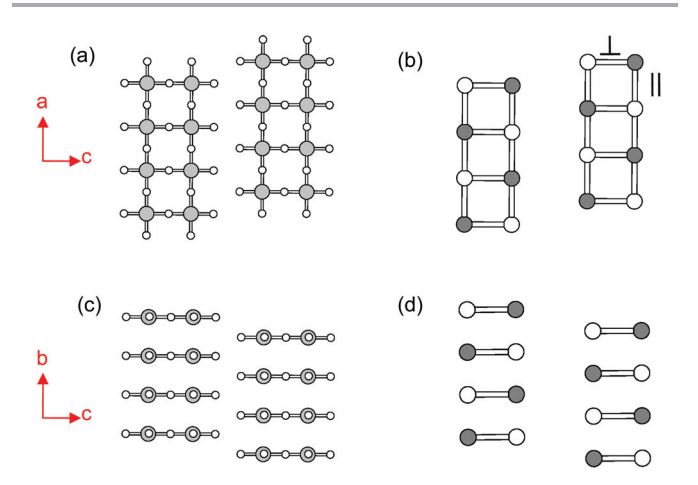


Fig. 9 Schematic projection views showing the Fe_2O_5 ladders of $Sr_3Fe_2O_5$ (a) along the a-direction and (b) along the b-direction. The AFM ordering in the Fe_2O_5 ladders of $Sr_3Fe_2O_5$ viewed (c) along the a-direction and (b) along the b-direction. In (a) and (b) the Fe atoms are indicated by large shaded circles. In (c) and (d) the shaded and unshaded circles represent up-spin and down-spin Fe^{2+} sites, respectively.

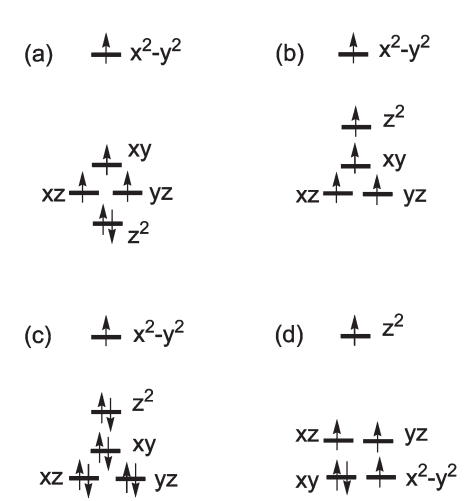


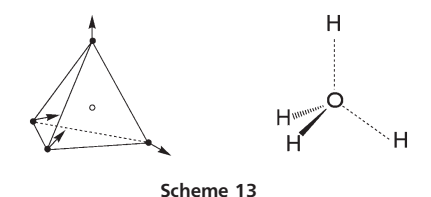
Fig. 10 The d-level splitting patterns of (a) a high-spin Fe^{2+} (d^6) ion in an FeO_4 square plane, (b) a high-spin Mn^{3+} (d^4) ion in an axially-elongated MnO_6 octahedron, (c) a Cu^{2+} (d^9) ion in an axially-elongated CuO_6 octahedron, (d) a high-spin Fe^{2+} (d^6) ion located at a linear coordinate site (D_{3d} local symmetry) of ($Me_3Si)_3C$ –Fe– $C(SiMe_3)_3$. The local z-axis is perpendicular to the FeO_4 square plane in (a), and along the elongated Mn–O and Cu–O bonds in (b) and (c), respectively, and along the C–Fe–C axis in (d).

because the magnetic orbitals xz and yz overlap directly through space across the Fe...Fe contact (3.503 Å).41 The latter situation is the same as that found for the 3D antiferromagnet SrFeO₂, 45,46 in which the FeO₂ sheets made up of cornersharing FeO₄ square planes stacked along the c-direction with Sr²⁺ ions in between adjacent FeO₂ sheets. Thus, in each 2D Fe₂O₅ slab, adjacent spin sites have a strong AFM coupling that doubles the cell along the a- and b-directions (Fig. 9b,d). The exchange interactions between adjacent Fe₂O₅ slabs vanish, since any given spin site of one slab is located above the center of an AFM rectangle $(J_{\perp}, J_a, J_{\perp}, J_a)$ of its adjacent slab. Consequently, as far as the spin exchange interactions are concerned, Sr₃Fe₂O₅ is a 2D AFM system and hence cannot undergo a 3D AFM order. 42 Experimentally, however, it undergoes a 3D AFM order at T_N = 296 K leading to a (2a, 2b, c) magnetic supercell.44

The additional interaction along the c-direction that $\mathrm{Sr_3Fe_2O_5}$ needs to undergo a 3D AFM order is provided by the MDD interaction, which is a long-range interaction. The MDD interaction is weak, being of the order of 0.1 meV for two spin-1/2 ions separated by 2 Å. Given two spins located at sites i and j with the distance r_{ij} and the unit vector \vec{e}_{ij} along the distance, the MDD interaction is described by 41

$$\left(\frac{g^2 \mu_{\rm B}^2}{a_0^3}\right) \left(\frac{a_0}{r_{ij}}\right)^3 \left[-3(\vec{S}_i \cdot \vec{e}_{ij})(\vec{S}_j \cdot \vec{e}_{ij}) + (\vec{S}_i \cdot \vec{S}_j)\right]$$
(30)

where a_0 is the Bohr radius (0.529177 Å) and $(g\mu_{\rm B})^2/(a_0)^3 = 0.725$ meV. The MDD effect on the preferred spin orientation of a given magnetic solid can be examined by comparing the MDD interaction energies calculated for a number of ordered spin arrangements. In summing the MDD interactions between various pairs of spin sites, it is necessary to employ



Perspective

the Ewald summation method. ⁴⁷ Calculations of the MDD interaction energies of $Sr_3Fe_2O_5$ with the spin orientations fixed along the a-, b- and c-directions (||a,||b and ||c, respectively) show that the relative stabilities of the spin orientations decrease in the order ||c|| > ||b|| > ||a|, namely, the spins of $Sr_3Fe_2O_5$ prefer the ||c|| > ||c|| > ||c||, the rung direction of the two-leg ladder). The same conclusion is reached in terms of the magnetic anisotropy energies determined from DFT + U calculations with SOC effects included (see Section 8B). ⁴¹

In discussing the 3D magnetic order and the spin orientation of a magnetic solid, the MDD interaction is often neglected. However, this interaction can become non-negligible especially when the spin S of a magnetic ion is large, because the MDD interaction is proportional to S^2 . For example, in the magnetic compounds Dy₂Ti₂O₇ and Ho₂Ti₂O₇, the rare-earth ions Ho3+ (f10) and Dy3+ (f9) form a pyrochlore spin lattice (Scheme 12 (top right)). The spin exchange between these ions should be negligible because their magnetic orbitals are given by their 4f orbitals. Given the pyrochlore spin lattice, the weak interactions between these ions are highly spin-frustrated. Nevertheless, at a very low temperature, Dy₂Ti₂O₇ and Ho₂Ti₂O₇ undergo a 3D long-range magnetic order because of the MDD interaction.⁴⁸ In the ordered magnetic structure, the spins in each tetrahedron of spin sites have a "two-in-two-out" orientation (Scheme 13 (left)), which resembles the arrangement of the two O-H bonds and two O···H hydrogen bonds around a H₂O molecule in ice (Scheme 13 (right)). Thus, Dy₂Ti₂O₇ and Ho₂Ti₂O₇ are known as spin ice systems.

C. Ferromagnetic and ferromagnetic-like transitions

For a magnetic system undergoing a FM phase transition below a critical temperature T_c , the magnetization \vec{M} as a function of temperature T shows a sharp increase below $T_{\rm c}$ and gradually approaches the saturation limit, as depicted in Fig. 11a. The magnetization \vec{M} as a function of magnetic field \vec{H} exhibits a hysteresis loop as shown in Fig. 11b. In the absence of a magnetic field, a FM system does not have a single FM domain but possesses a large number of smaller FM domains such that the spin arrangement within each domain is FM, but that between adjacent domains is not (Fig. 11c). 49 As the field increases, the spins of each FM domain gradually begin to line up with the field and the domains with more lined-up spins increase in size, eventually forming one domain with completely lined-up spins and hence reaching the magnetization saturation. When the field decreases from the saturation point, the reversal of the above process takes place. The hysteresis of the \overrightarrow{M} vs. \overrightarrow{H} curves shows that the field-induced domain change proceeds more slowly when the field is

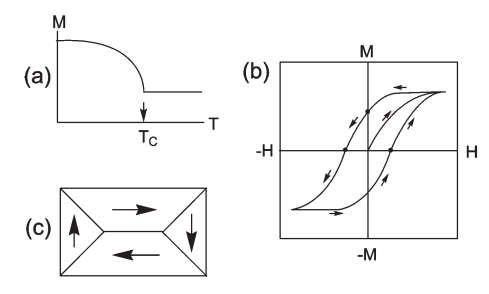
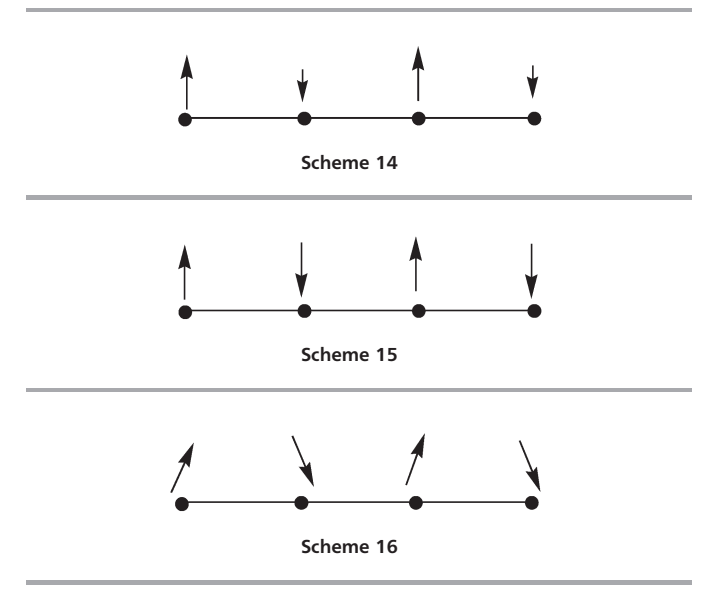


Fig. 11 Representative properties of a magnetic system undergoing a ferromagnetic transition below T_c . (a) Magnetization *versus* temperature. (b) Magnetization *versus* magnetic field measured at a low temperature below T_c . (c) Ferromagnetic domains of a sample with different spin directions.



decreased than increased. The MDD interaction, which is a long-range interaction, is energetically unfavorable for a single FM domain. To avoid this unfavorable long-range MDD interaction, the system develops a large number of smaller FM domains with different spin orientations. ⁴⁹ The non-FM spin arrangements between the domain boundaries are energetically unfavorable in terms of spin exchange interactions, but the removal of a single-domain FM order is energetically favorable in terms of the MDD interaction. In FM materials, the MDD interaction overcomes the unfavorable effect of the non-FM spin arrangements along the boundaries between adjacent FM domains.

A ferrimagnetic system, which contains two types of magnetic ions with different moments, undergoes an AFM ordering between the two types of ions (Scheme 14) and as a result generates a net nonzero moment. An AFM system (Scheme 15) can generate a small net moment when its moments undergo spin canting (Scheme 16), because it generates small net magnetic moments at the spin sites (Scheme 17). The spin canting arises from the DM interaction (see Section 9).⁵⁰ The occurrence of spin canting in an AFM system is signaled by a sharp increase in the magnetic susceptibility at a low temperature. Below a certain low temperature, the magnetic susceptibility of a compound may depend on whether or not a magnetic field

Dalton Transactions Perspective



is applied to its powder sample while it is being cooled. In such a case, a field-cooled (FC) sample generally exhibits a higher susceptibility than does a zero-field-cooled (ZFC) sample, which can occur when the sample undergoes a weak spin canting below a certain temperature hence acquiring a weak FM character.

D. Typical cases leading to ferromagnetic interaction

It is of interest to examine the typical situations leading to FM spin exchanges. Our discussion in Section 4A shows that, to have a FM spin exchange J_1 , its J_2 component should be stronger than its AFM component J_{AF} , namely, the overlap density between the magnetic orbitals involved should be large but the overlap integral between them should be small. An orbital ordering (equivalently, a cooperative Jahn-Teller distortion) leading to a FM exchange is related to the above observation. In the perovskite fluoride KCuF₃ made up of corner-sharing CuF₆ octahedra, ⁵¹ each CuF₆ octahedron containing a Cu²⁺ ion undergoes a Jahn-Teller distortion to have short, medium and long Cu-F distances (hereafter, Cu-F_s, Cu-F_m, and Cu-F_l, respectively). Each CuF₆ octahedron has the linear F_m-Cu-F_m unit along the c-direction, sharing the F_m atoms between adjacent CuF₆ octahedra. In the ab-plane, each CuF₆ octahedron has the linear F_s-Cu-F_s and F_l-Cu-F_l units perpendicular to each other, and the Cu-F_s bonds of one CuF₆ octahedron are corner-shared with the Cu-F₁ bonds of its adjacent CuF₆ octahedra (Fig. 12a). Let us consider this cooperative Jahn-Teller distortion (or orbital order)⁵² from the viewpoint of an ideal CuF₆ octahedron for which, by considering only the electrons at the e_g level, the electron configuration is given by $(x^2 - y^2)$, $(z^2)^3$. Since the $(x^2 - y^2)^3$ and $(z^2)^3$, to be precise) orbitals are degenerate, one can generate an alternative representation from their linear combinations

$$(3z^2 - r^2) + (x^2 - y^2) \rightarrow (z^2 - x^2, z^2 - y^2)$$
 (31)

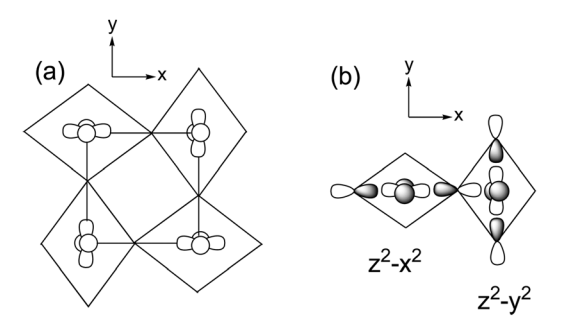


Fig. 12 (a) The arrangement of the $z^2 - x^2$ and $z^2 - y^2$ orbitals of the Cu²⁺ ions CuF_4 layer (parallel to the ab-plane) of $KCuF_3$ in the orbital-ordered state. (b) The arrangement of the $z^2 - x^2$ and $z^2 - y^2$ orbitals of two adjacent Cu²⁺ sites in the CuF₄ layer in the orbital-ordered state, showing the presence of strong overlap density between them hence leading to a FM spin exchange.

In the structure with the cooperative Jahn-Teller distortion (Fig. 12a), the degeneracy of the $z^2 - x^2$ and $z^2 - y^2$ levels at each CuF₆ octahedron is lifted. For each CuF₆ octahedron with the Cu-F₁ bonds along the x-direction, the $z^2 - x^2$ is lower in energy than the $z^2 - y^2$ level so that the $z^2 - x^2$ is doubly occupied, and the $z^2 - y^2$ level is singly occupied to become the magnetic orbital. The opposite happens for each CuF₆ octahedron with the Cu-F_s bonds along the x-direction. Consequently, the magnetic orbitals are orthogonally ordered as depicted in Fig. 12a. In this orbital ordered state, the spin exchange between neighboring sites is FM. It should be recalled that the $z^2 - x^2$ and $z^2 - y^2$ magnetic orbitals have the F 2p orbital tails as indicated in Fig. 12b. Therefore, given the $z^2 - x^2$ and $z^2 - y^2$ magnetic orbitals on adjacent Cu²⁺ sites, the overlap integral between them is zero by symmetry while the overlap density between them, which involves the F 2p tail of one magnetic orbital and the Cu 3d head of the other magnetic orbital (Fig. 12b), is substantial because of the short Cu-F_s distance involved.

For magnetic oxides with mixed-valent magnetic ions M and M', the M-O-M' spin exchange is commonly referred to as the double exchange,⁵³ which can be either FM or AFM. We distinguish two different cases of double exchange. Let us first consider the case when the local structures of the spin sites are identical so that, as depicted in Fig. 13a for high-spin Mn³⁺ (d4) and Mn4+ (d3) ions in octahedral environments, their d-block levels can be treated as identical. The strength of the hopping integral t between the spin sites is determined largely by the interaction between their eg magnetic orbitals because the latter arise from σ^* -antibonding between the Mn 3d and O 2p orbitals. If the two adjacent Mn³⁺ and Mn⁴⁺ spins have a FM arrangement (Fig. 13a), the filled $e_g \uparrow$ level of the Mn³⁺ site and the empty e_g↑ level of the Mn⁴⁺ site are identical in energy so that the electron hopping from the Mn³⁺ to the Mn⁴⁺ site involves a degenerate orbital interaction. If the two adjacent Mn³⁺ and Mn⁴⁺ spins were to have an AFM arrangement (Fig. 13b), the filled $e_g \uparrow$ level of the Mn^{3+} site would be well separated from the empty $e_g \uparrow$ level of the Mn^{4+} site (see Fig. 2). Thus, the electron hopping from the Mn³⁺ to the Mn⁴⁺ site involves a non-degenerate orbital interaction. Consequently, between adjacent Mn³⁺ to the Mn⁴⁺ ions, the FM arrangement is energetically more favorable than the AFM arrangement. This hopping gives rise to mobile electrons, and hence to metallic conductivity.

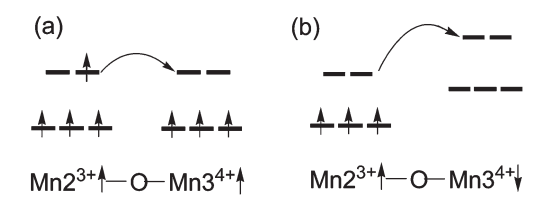


Fig. 13 Interaction between two Mn³⁺ and Mn⁴⁺ sites (in octahedral environments) linked by a Mn-O-Mn bridge in the (a) FM and (b) AFM arrangements of their spins. Here it is assumed that Mn³⁺O₆ and Mn⁴⁺O₆ octahedra have the

We now examine the case when mixed-valent spin sites possess different local structures by considering one specific Mn-O-Mn spin exchange interaction of CaMn₇O₁₂, which has three non-equivalent Mn atoms, i.e., Mn1, Mn2 and Mn3. The spin exchange between the high-spin Mn2³⁺ (d⁴) and Mn3⁴⁺ (d³) ions has the $\angle Mn2^{3+}$ -O-Mn3⁴⁺ angle of 137.6° (Fig. 14a), 54,55a in which the Mn2³⁺ (d⁴) ion forms an axiallycompressed MnO₆ octahedron, and the Mn3⁴⁺ (d³) ion a nearly ideal MnO6 octahedron. The local coordinates around the $Mn2O_6$ and $Mn3O_6$ octahedra are described by (x, y, z) and (x', y, z)y', z'), respectively. If the two adjacent Mn2³⁺ and Mn3⁴⁺ spins have a FM arrangement, there is a small energy gap between the filled $x^2 - y^2$ level of the Mn2³⁺ site and the empty $x'^2 - y'^2$ level of the Mn3⁴⁺ site (Fig. 15).⁴⁸ This energy gap would be greater if the two adjacent Mn3+ and Mn4+ spins were to have an AFM arrangement (see Fig. 2). In terms of this energy gap consideration, the FM arrangement is favored over the AFM arrangement. However, the ∠Mn2³⁺-O-Mn3⁴⁺ angle of this exchange path is rather large (137.6°), so that the overlap integral as well as the overlap density between the O 2p tails of the two $x^2 - y^2$ magnetic orbitals at the shared O atom are both strong (Fig. 14b), leading to the competition of the $J_{\rm F}$ and $J_{\rm AF}$ contributions. Indeed, DFT + U calculations for CaMn₇O₁₂ with U^{eff} on Mn show that this exchange is FM when U^{eff} is greater than a certain value (i.e., ~3 eV), but is AFM otherwise. 55a This is understandable because the J_{AF} term is diminished with increasing U^{eff} (see eqn (16b)).

For the spin exchange between Mn2³⁺ (d⁴) and Mn3⁴⁺ (d³) ions in CaMn₇O₁₂ discussed above, we note that the O 2p tail of the $x^2 - y^2$ magnetic orbital of the Mn³⁺ ion also overlaps well with that of the x'z' magnetic orbital of the Mn^{4+} ion (Fig. 14c). As will be discussed later, this gives rise to a very strong DM interaction between the Mn2³⁺ and Mn3⁴⁺ sites (see Section 9A for further discussion). 55a

E. Short range order

2D, 1D and zero-dimensional (0D) magnetic systems described by a Heisenberg spin Hamiltonian cannot have a long-range magnetic order. Due to the absence of a long-range magnetic order, these systems exhibit no λ -type anomaly in the temperature-dependence of $C_{p,mag}$. Nevertheless, they can exhibit short-range order, namely, patches with AFM order are made

and broken dynamically with no communication between different ordered patches. The occurrence of such a shortrange order in a uniform Heisenberg AFM chain described by the NN AFM exchange J (Scheme 18 (left)) is manifested by the presence of an extended broad maximum in the χ vs. T plot (Scheme 18 (right)). For a Heisenberg AFM uniform chain made up of spin S ions with NN spin exchange J, suppose that the magnetic susceptibility maximum χ_{max} occurs at temperature T_{max} . Then, the spin exchange J is related to the T_{max} as⁵⁶

$$\frac{k_{\rm B}T_{\rm max}}{|I|} = C \tag{32}$$

where the constant C = 0.641 for $S = \frac{1}{2}$, 1.35 for S = 1, 2.38 for S = 3/2, 3.55 for S = 2, and 5.30 for S = 5/2.

A magnetic system that is primarily a 1D AFM chain may possess weak interchain interactions in the remaining two directions. In such a case, the system will exhibit a short-

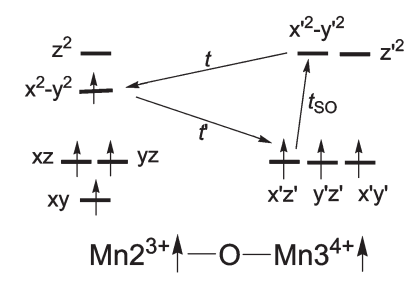
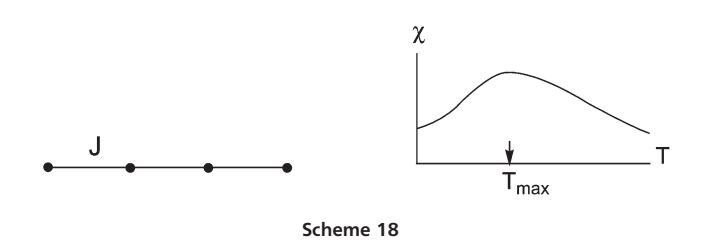


Fig. 15 The d-block levels of the axially compressed Mn2O₆ octahedron and the nearly ideal Mn3O₆ octahedra forming the Mn2³⁺–O–Mn3⁴⁺ exchange path with $\angle Mn2^{3+}$ –O-Mn3⁴⁺ = 137.6° in CaMn₇O₁₂. The energy levels are given assuming that the Mn2³⁺ and Mn3⁴⁺ spins have a FM arrangement. The $x^2 - y^2$ magnetic orbital of Mn2³⁺ interacts strongly with the $x'^2 - y'^2$ magnetic orbital of Mn3⁴⁺ and also with the x'z' magnetic orbital of Mn3⁴⁺. At the Mn3⁴⁺ site the $x'^2 - y'^2$ magnetic orbital interacts with the x'z' magnetic orbital by SOC.



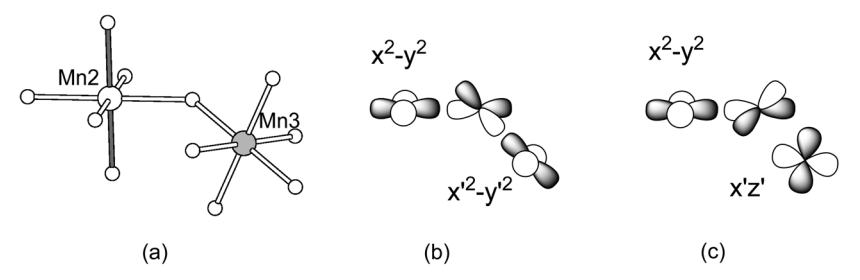


Fig. 14 The spin exchange between the high-spin $Mn2^{3+}$ (d^4) and $Mn3^{4+}$ (d^3) ions. (a) A perspective view of the exchange path between the $Mn2^{3+}$ (d^4) and $Mn3^{4+}$ (d³) ions. The short Mn2–O bonds of the axially-compressed Mn2O₆ octahedron are shaded. (b) The arrangement of the O 2p tails of the $x^2 - y^2$ magnetic orbital of Mn2³⁺ and the $x'^2 - y'^2$ magnetic orbital of Mn3⁴⁺ at the O atom of the Mn2³⁺-O-Mn3⁴⁺ bridge. (c) The arrangement of the O 2p tails of the $x^2 - y^2$ magnetic orbital of Mn2³⁺ at the O atom of the Mn2³⁺-O-Mn3⁴⁺ bridge. netic orbital of Mn2³⁺ and the x'z' magnetic orbital of Mn3⁴⁺ at the shared O atom of the Mn2³⁺-O-Mn3⁴⁺ bridge.

Dalton Transactions Perspective

range-order behavior, which is then followed by a 3D long range order. The entropy change ΔS determined from the associated $C_{\rm p,mag}$ νs . T curve is smaller than $R \ln(2S+1)$, because the system has lost some entropy due to the shortrange order. That is, the 3D order in such a case is an order of the short-range-ordered segments.

7. Energy gap in the magnetic energy spectrum

A. Spin gap and field-induced magnetic order

The χ vs. T plot of a uniform Heisenberg AFM chain shows that the susceptibility at T=0 is nonzero (Scheme 18 (right)), which is due to the fact that there is no energy gap between the magnetic ground and excited states. This is true for a 1D Heisenberg uniform AFM chain made up of half-integer-spin ions. However, this is not the case for the chains made up of integer-spin ions according to the Haldane conjecture, ⁵⁷ which predicts that there is an energy gap between the magnetic ground and excited states. Indeed, experimentally, the quasi 1D Heisenberg antiferromagnet Ni(C₂H₈N₂)₂NO₂(ClO₄), containing uniform chains of S=1 Ni²⁺ ions, is found to have a spin gap. ⁵⁸

Certain AFM systems made up of half-integer-spin ions have a substantial energy gap between the magnetic ground and excited states. For example, consider a spin dimer with AFM spin exchange J. If the magnitude of the exchange J is large and the applied magnetic field is weak, the lowest Zeeman split level (*i.e.*, the $S_z = -1$ level) of the triplet state is still well above the singlet state so that, below a certain temperature, the available thermal energy $k_{\rm B}T$ is not large enough to thermally populate the $S_z = -1$ level (Fig. 16a). Consequently, the magnetic susceptibility becomes zero below a certain temperature (Scheme 19). Namely, an AFM spin dimer

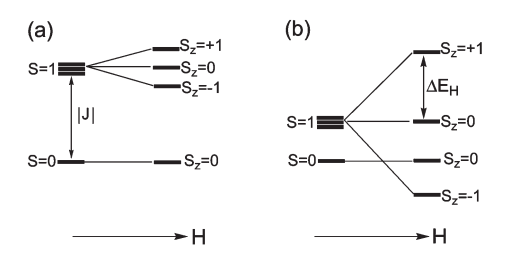
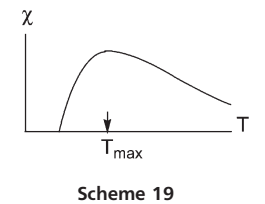
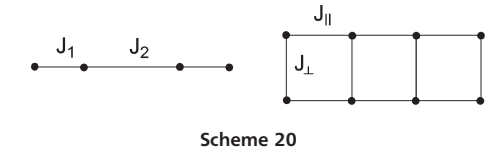


Fig. 16 Effect of magnetic field on the energy levels of an AFM spin dimer made up of two S = 1/2 ions for (a) a large and (b) a small energy difference between the singlet and triplet states.





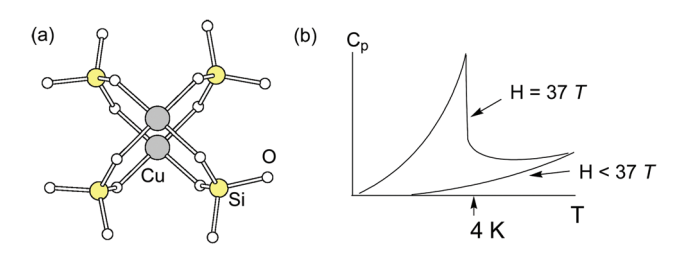


Fig. 17 (a) A spin dimer unit of BaCuSi₂O₆, in which two CuO₄ square planes are stacked on top of each other and are corner-shared with four SiO₄ tetrahedra. (b) The specific heat of BaCuSi₂O₆ measured in the absence and presence of a strong magnetic field. It shows a λ -like anomaly when the applied magnetic field is greater than 34 T, thereby showing a field-induced 3D ordering in BaCuSi₂O₆.

is a spin-gapped system. Other representative spin-gap systems include a Heisenberg alternating chain (Scheme 20 (left)) with two different spin exchanges (AFM J_1 and AFM J_2 , or AFM J_1 and FM J_2) and a two-leg spin ladder with AFM rung and leg spin exchanges (J_{\perp} and J_{\parallel}), respectively) (Scheme 20 (right)).

A magnetic system consisting of AFM spin dimers, being a 0D magnetic system, cannot undergo a 3D long range order. 42 An interesting situation occurs for an AFM spin dimer with small J when a large magnetic field is applied. In such a case, the $S_z = -1$ level of the triplet state becomes lower in energy than the $S_z = 0$ level of the singlet state (Fig. 16b). As a result, the spin dimer behaves as an integer-spin (i.e., Bose-Einstein) system. This means that all spin dimers can have the same lowest-energy state, namely, the magnetic system now has a 3D long range order although there is no interaction between the spin dimers. Such a field-induced 3D ordering occurs in BaCuSi₂O₆, ^{59,60} in which each spin dimer is made up of two CuO₄ square planes stacked on top of each other and cornershared with four SiO₄ tetrahedra (Fig. 17a). The Cu-O···Si⁴⁺···O-Cu spin exchange is weak, so that the spin exchange J for this spin dimer is weak. The specific heat measurements on BaCuSi₂O₆ show a λ -like anomaly when the applied magnetic field is greater than 34 T, thereby showing a field-induced 3D ordering in BaCuSi₂O₆ (Fig. 17b).⁶⁰

B. Magnetization plateaus

Let us examine the energy spectrum of a magnetic system from the viewpoint of its allowed energies under a magnetic field by considering an AFM spin dimer. As depicted in Fig. 16, the singlet state is unaffected by the magnetic field but the triplet state is split into three levels by the field. The energy difference ΔE_H between the adjacent Zeeman split levels increases continuously from zero at H=0 with increasing H. Therefore, the allowed energy spectrum of the spin

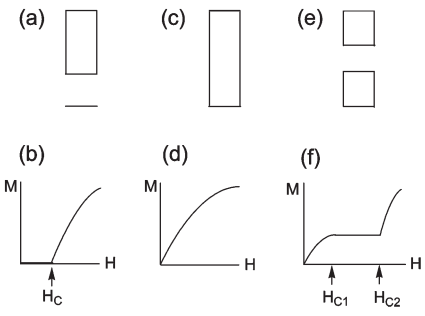
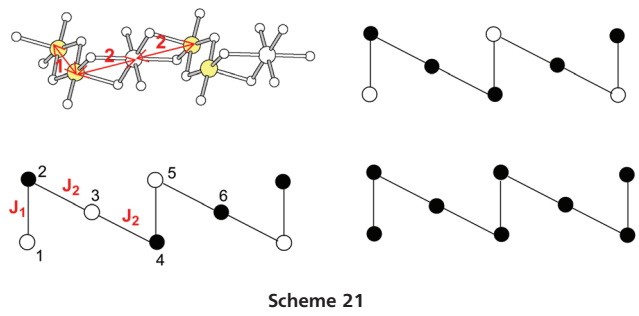


Fig. 18 Schematic diagrams showing how the magnetization plateau is related to an energy gap of the energy spectrum that a magnetic system can have under a magnetic field. A spin gap in the energy spectrum, (a), leads to the zero magnetization plateau, (b). A magnetic system with no energy gap, (c), shows no magnetization plateau, (d). An energy gap in the middle of the energy spectrum, (e), leads to a finite magnetization plateau, (f).

dimer under a magnetic field can be depicted as in Fig. 18a, where it is assumed that the field is not strong enough for the $S_z = -1$ level of the triplet state to reach the $S_z = 0$ level of the singlet ground state. The energy band associated with the triplet state indicates the region of energy that can be reached continuously by increasing the field H; the allowed energies of the triplet are given by the midpoint of the band at H = 0, and sweep toward the band bottom and the band top with increasing H from 0. The magnetization M of the above spin dimer as a function of H at a very low temperature behaves as shown in Fig. 18b, which shows M = 0 until H reaches a critical value H_c because, at field H smaller than H_c , the system cannot reach the bottom of the triplet band so that M = 0. Once $H > H_c$, M increases gradually with increasing H. The flat region of the M vs. H plot is known as the magnetization plateau. Since this plateau occurs at M = 0, it is a zero magnetization plateau. All spin-gap systems should show a zero magnetization plateau. If the energy spectrum of a magnetic system under a magnetic field has no energy gap (Fig. 18c), the M increases gradually with increasing H with no magnetization plateau until the magnetization reaches its saturation value (Fig. 18d).

It should be noted that the energy bands of a magnetic system under a magnetic field may possess an energy gap in the middle of the energy spectrum (Fig. 18e). In such a case the magnetization plateau of the M vs. H plot occurs at a nonzero M value (i.e., a finite magnetization plateau) between two critical magnetic fields H_{c1} and H_{c2} (Fig. 18f). Such a finite magnetization plateau is found for a low-dimensional AFM system such as $Cu_3(P_2O_6OH)_2^{61,62}$ and $Cu_3(CO_3)_2(OH)_2^{63,64}$ which exhibit a 1/3 magnetization plateau. The oxide Cu₃(P₂O₆OH)₂ consists of zigzag AFM chains of Cu²⁺ ions depicted in Scheme 21 (top left) (where the large yellow and white circles represent Cu2 and Cu1 atoms, respectively), and these chains interact to give rise to 2D magnetic character. 62 Nevertheless, the 1/3 magnetization plateaus can be readily understood by considering this 1D AFM chain defined by two spin exchanges J_1 and J_2 . The repeat unit of this AFM chain has six spin-1/2 Cu²⁺ ions with the magnetic bond sequence of J_1 – J_2 – J_2 – J_1 – J_2 – J_2 . The AFM arrangement (Scheme 21 (bottom



left)) has zero net moment so the average moment m per spin site is zero. J_2 is considerably weaker than J_1 (i.e., $J_2/J_1 \approx 1/6$), 62 so the spin moments at the sites making only J_2 magnetic bonds will be broken first to eventually line up with the field H as the latter increases from zero. This leads to the initial increase in M with increasing H. The magnetic structure corresponding to the 1/3 magnetization plateau is depicted in Scheme 21 (top right), in which the spin at site 3 is flipped so that m = 1/3. The spin flips at sites 1 and 5 will lead to the saturation magnetization (m = 1) (Scheme 21 (bottom right)). However, the J_1 magnetic bond is strong so that this does not happen unless the field is stronger than a critical value H_{c2} . This explains why a 1/3 magnetization plateau occurs between H_{c1} and H_{c2} . For an AFM chain made up of spin-S magnetic ions with n sites per magnetic unit cell, the average magnetization per site *m* is predicted to occur if n(S - m) = integer.⁶⁵

Manifestations of spin-orbit coupling

A. Spin orientation

Experimentally, the spin orientations of a magnetic solid are determined by neutron diffraction measurements. From the viewpoint of theory, the spin orientation in coordinate space is set by SOC, which for an atom with many unpaired electrons and total spin S is expressed as

$$\hat{H}_{SO} = \lambda \hat{S} \cdot \hat{L},\tag{33}$$

where the SOC constant λ is positive if the electron shell containing unpaired electrons is less than half-filled [e.g., V⁴⁺ (d¹)], but is negative if the shell is more than half-filled $[e.g., Cu^{2+}(d^9)]$. The lowest-energy spin-orbit coupled state for $\lambda > 0$ is obtained when \vec{L} and \vec{S} are antiparallel leading to $\vec{J} = \vec{S} - \vec{L}$, but that for $\lambda < 0$ when \vec{L} and \vec{S} are parallel leading to $\vec{J} = \vec{S} + \vec{L}$. In a magnetic solid the magnetic moment of each spin site results from the spin moment interacting with the unquenched orbital moment under \hat{H}_{SO} . In general, the magnitude of λ increases on going from 3d to 4d to 5d in a given family of transition-metal atoms, and also with increasing the oxidation state for a given nd element. 40,66

An important consequence of SOC is that the spin gets a preferred orientation in space with respect to the crystal lattice. Before we examine how this comes about, it is Dalton Transactions Perspective

necessary to recall that the orbital angular momentum states $|L,L_z\rangle$ follow the relationships

$$\hat{L}_z|L, L_z\rangle = L_z|L, L_z\rangle$$

$$\hat{L}_+|L, L_z\rangle = \sqrt{L(L+1) - L_z(L_z+1)}|L, L_z+1\rangle$$

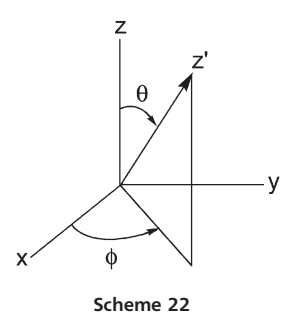
$$\hat{L}_-|L, L_z\rangle = \sqrt{L(L+1) - L_z(L_z-1)}|L, L_z-1\rangle$$
(34)

where the ladder operators are given by $\hat{L}_+ = \hat{L}_x + iLI_y$ and $\hat{L}_+ = \hat{L}_x - iLI_y$. The spin states $|S, S_z\rangle$ follow the analogous relationships as discussed earlier (eqn (8)). These relationships play an important role in our discussion of SOC and spin orientation in space (see Section 9A).

To gain insight into how the $\hat{S}\cdot\hat{L}$ term governs the spin orientation in space, it is necessary to employ two independent coordinate systems, *i.e.*, (x, y, z) for \hat{L} and (x', y', z') for \hat{S} . Then, the preferred spin direction z' is described by the two angles (θ, ϕ) , where θ and ϕ are the azimuthal and polar angles of the preferred spin direction with respect to the (x, y, z) coordinate system (Scheme 22). As a consequence, the $\hat{H}_{SO} = \lambda \hat{S}\cdot\hat{L}$ term is written as^{40,67}

$$\begin{split} \hat{H}_{SO} &= \lambda \hat{S}_{z'} \left(\hat{L}_z \cos \theta + \frac{1}{2} \hat{L}_+ e^{-i\varphi} \sin \theta + \frac{1}{2} \hat{L}_- e^{i\varphi} \sin \theta \right) \\ &+ \frac{\lambda}{2} \hat{S}_{+} \cdot \left(-\hat{L}_z \sin \theta - \hat{L}_+ e^{-i\varphi} \sin^2 \frac{\theta}{2} + \hat{L}_- e^{i\varphi} \cos^2 \frac{\theta}{2} \right) \\ &+ \frac{\lambda}{2} \hat{S}_{-} \cdot \left(-\hat{L}_z \sin \theta + \hat{L}_+ e^{-i\varphi} \cos^2 \frac{\theta}{2} - \hat{L}_- e^{i\varphi} \sin^2 \frac{\theta}{2} \right). \end{split}$$
(35)

This expression shows how the SOC energy depends on the spin orientation (θ, ϕ) . To determine the energetically favorable spin orientation of a magnetic solid, one can determine its total energy on the basis of DFT + U + SOC calculations as a function of the spin orientation.⁶⁸ Then, the preferred spin orientation is the direction that provides the lowest total energy. Experimentally, neutron diffraction refinements at a very low temperature provide information about the magnitudes and orientations of the moments at the spin sites of a magnetic solid. In the following discussion of the preferred spin orientation, it is convenient to express the d-levels $x^2 - y^2$, xy, yz, xz and z^2 in terms of the spherical harmonics $Y_l^m(m = -2, -1, 0, 1, 2)$ as shown below (note that the l and m values of the spherical harmonics Y_l^m correspond to L and L_z values, respectively).



$$x^{2} - y^{2} \propto (Y_{2}^{2} + Y_{2}^{-2})/\sqrt{2}$$

$$xy \propto -i(Y_{2}^{2} - Y_{2}^{-2})/\sqrt{2}$$

$$yz \propto i(Y_{2}^{1} + Y_{2}^{-1})/\sqrt{2}$$

$$xz \propto -(Y_{2}^{1} - Y_{2}^{-1})/\sqrt{2}$$

$$z^{2} \propto Y_{2}^{0}$$
(36)

On the basis of the m values, the d-states can be classified in terms of d_m ($m = \pm 2, \pm 1, 0$) so that we have the following equivalences:

$$(x^{2} - y^{2}, xy) \leftrightarrow (d_{2}, d_{-2})$$

$$(xz, yz) \leftrightarrow (d_{1}, d_{-1})$$

$$z^{2} \leftrightarrow d_{0}$$

$$(37)$$

For a qualitative discussion of spin orientation, it is convenient to rewrite the SOC Hamiltonian \hat{H}_{SO} as

$$\hat{H}_{SO} = \hat{H}_{SO}^0 + \hat{H}_{SO}^{'} \tag{38}$$

where \hat{H}_{SO}^0 is the "spin-conserving" term (*i.e.*, the first line of eqn (35)),

$$\hat{H}_{SO}^{0} = \lambda \hat{S}_{z'} \left(\hat{L}_{z} \cos \theta + \frac{1}{2} \hat{L}_{+} e^{-i\varphi} \sin \theta + \frac{1}{2} \hat{L}_{-} e^{i\varphi} \sin \theta \right), \quad (39)$$

and \hat{H}'_{SO} is the "spin-non-conserving" term (*i.e.*, the second and third lines of eqn (35)),

$$\hat{H}'_{SO} = \frac{\lambda}{2} \hat{S}_{+} \left(-\hat{L}_{z} \sin \theta - \hat{L}_{+} e^{-i\varphi} \sin^{2} \frac{\theta}{2} + \hat{L}_{-} e^{i\varphi} \cos^{2} \frac{\theta}{2} \right)
+ \frac{\lambda}{2} \hat{S}_{-} \left(-\hat{L}_{z} \sin \theta + \hat{L}_{+} e^{-i\varphi} \cos^{2} \frac{\theta}{2} - \hat{L}_{-} e^{i\varphi} \sin^{2} \frac{\theta}{2} \right).$$
(40)

The preferred spin orientation can be understood on the basis of perturbation theory by treating these SOC Hamiltonians as perturbations with the split d-block levels of a magnetic ion as unperturbed states. When an occupied d-level $i = \psi_{\text{o}} \uparrow \text{ (or } \psi_{\text{o}} \downarrow)$ with energy e_i interacts with an unoccupied d-level $j = \psi_{\text{u}} \uparrow \text{ (or } \psi_{\text{u}} \downarrow)$ with energy e_j via the matrix element $\langle i | \hat{H}_{\text{SO}}^0 | j \rangle$, the associated energy lowering is given by

$$\Delta E_{\rm SOC} = -\frac{\left| \langle i | \hat{H}_{\rm SO}^0 | j \rangle \right|^2}{\left| e_i - e_j \right|} \tag{41a}$$

(Here $|\langle i|\hat{H}_{SO}^0|j\rangle|^2$ represents $\langle i|\hat{H}_{SO}^0|j\rangle\langle j|\hat{H}_{SO}^0|i\rangle$.) When an occupied d-level $i=\psi_0\uparrow$ with energy e_i interacts with an unoccupied d-level $j=\psi_u\downarrow$ with energy e_j via the matrix element $\langle i|\hat{H}_{SO}^i|j\rangle$, the associated energy lowering is given by

$$\Delta E_{\text{SOC}} = -\frac{\left| \langle i | \hat{H}'_{\text{SO}} | j \rangle \right|^2}{\left| e_i - e_j \right|} \tag{41b}$$

In determining the preferred spin orientation, the most important interaction between occupied and unoccupied spin levels is the one with the smallest energy gap $\Delta e = (e_i - e_j)$. The d-levels of the same |m| values (e.g., between xz and yz, and between xy and $x^2 - y^2$) interact through the operator \hat{L}_z to give nonzero $\langle i|\hat{H}_{SO}^i|j\rangle$ and $\langle i|\hat{H}_{SO}^i|j\rangle$. The d-levels of different m values with $|\Delta m| = 1$ (e.g., between xz/yz and $xy/(x^2 - y^2)$, and

between z^2 and xz/yz) interact through the ladder operators \hat{L}_+ and \hat{L}_- to give nonzero $\langle i|\hat{H}_{\rm SO}^0|j\rangle$ and $\langle i|\hat{H}_{\rm SO}^\prime|j\rangle$. The z^2 orbital cannot interact with the $xy/(x^2 - y^2)$ orbitals under SOC because their *m* values differ by $|\Delta m| = 2$.

To illustrate the use of eqn (41a), we consider two examples. The high-spin Fe²⁺ (d⁶) ions of the FeO₄ square planes in Sr₃Fe₂O₅ 41,43,44 and SrFeO₂ 45,46 exhibit easy-plane anisotropy (i.e., the $\theta = 90^{\circ}$ spin orientation), while the high-spin Mn³⁺ (d⁴) ions of axially-elongated MnO₆ octahedra in TbMnO₃ ^{69,70} and $Ag_2MnO_2^{71}$ show easy-axis anisotropy (i.e., the $\theta = 0^{\circ}$ spin orientation). The high-spin Fe²⁺ (d⁶) ion of an FeO₄ square plane has the d-state splitting pattern $(z^2)^2 < (xz, yz)^2 < (xy)^1 <$ $(x^2 - y^2)^1$ (Fig. 10a). In the spin-polarized description associated with DFT + U calculations, 41,44 this splitting pattern is equivalent to

$$(z^2\uparrow)^1<(xz\uparrow,yz\uparrow)^1<(xy\uparrow)^1<(x^2-y^2\uparrow)^1$$

$$<(z^2\downarrow)^1<(xz\downarrow,yz\downarrow)^0<(xy\downarrow)^0<(x^2-y^2\downarrow)^0.$$

Namely, for the high-spin Fe2+ (d6) ion, the lowest energy gap between the occupied and unoccupied levels occurs between the $z^2\downarrow$ and the $xz\downarrow/yz\downarrow$ levels. Since these levels differ in their m values by ± 1 , they can interact when the spin is perpendicular to the orbital z-axis (i.e., $\theta = 90^{\circ}$). Namely, the preferred spin orientation of the Fe²⁺ ion is perpendicular to the z-axis (i.e., easy-plane anisotropy). For the high-spin Mn^{3+} (d⁴) ion of an axially-elongated MnO6 octahedron (with the z-axis taken along the elongated Mn-O bond) (Fig. 10b), the Mn³⁺ ion has the d-state splitting pattern^{70,71}

$$(xz\uparrow,yz\uparrow)^1<(xy\uparrow)^1<(z^2\uparrow)^1<(x^2-y^2\uparrow)^0,$$

so that the lowest energy gap between occupied and unoccupied levels occurs between the $z^2 \uparrow$ and $(x^2 - y^2) \uparrow$ levels. However, these two cannot interact under \hat{H}_{SO}^{0} because their m values differ by $|\Delta m| = 2$. The next lowest energy gap occurs for the $xy\uparrow$ and the $x^2 - y^2\uparrow$ levels, for which $|\Delta m| = 0$, and hence can interact if $\theta = 0^{\circ}$. Namely, the preferred spin direction is parallel to the orbital z-axis (i.e., easy-axis anisotropy).

To illustrate the use of eqn (41b), we consider the Cu²⁺ (d⁹, S = 1/2) ion of a CuO₄ square plane (or an axially elongated CuO_6 octahedron) with the d-electron configuration $(xz, yz)^4$ $(xy)^2 < (z^2)^2 < (x^2 - y^2)^1$ (Fig. 10c). In the spin-polarized description associated with DFT + U calculations, this splitting pattern means the sequence $(xz\uparrow,yz\uparrow)^2 < (xy\uparrow)^1 < (z^2\uparrow)^1 < (x^2 - yz\uparrow)^2$ $(xz)^{1}$ for the up-spin d-states, and the sequence (xz), $(yz)^{2}$ $(xy\downarrow)^1 < (z^2\downarrow)^1 < (x^2 - y^2\downarrow)^0$ for the down-spin d-states. According to the spin-polarized DFT + U calculations for compounds consisting of CuL₄ (L = O, Cl, Br) square planes (e.g., LiCuVO₄, ^{31,32} Bi₂CuO₄, ^{72,73} CuCl₂ ^{72,74} and CuBr₂ ^{72,75}), the upspin and down-spin d-states overlap in energy substantially such that the energy gap between $(x^2 - y^2 \uparrow)^1$ and $(x^2 - y^2 \downarrow)^0$ is considerably smaller than the gap the $(x^2 - y^2\downarrow)^0$ level makes with any other down-spin d-levels.⁶⁴ Therefore, the spin orientation will be governed by \hat{H}'_{SO} rather than by \hat{H}^0_{SO} , and the energy-lowering associated with \hat{H}'_{SO} is maximum when $\theta = 90^{\circ}$ (eqn (41b)). Thus the Cu²⁺ spin of a CuL₄ square plane is predicted to have easy-plane anisotropy. This prediction is in agreement with results of direct DFT + U + SOC calculations for LiCuVO₄, Bi₂CuO₄, CuCl₂ and CuBr₂.⁷² See below for further discussion.

B. Single-ion anisotropy

The preferred spin orientation of a magnetic ion leads to its single-ion magnetic anisotropy (or magnetocrystalline anisotropy). The simplest way of describing this magnetic anisotropy in terms of a spin Hamiltonian is to introduce the term $A_i \hat{S}_{iz}^2$ for each magnetic ion i into a spin Hamiltonian. ⁴⁶ Here the spin \hat{S}_{iz} is defined by the local z-axis of each ion i, and the constant A_i is related to the energy difference between the ||z|and $\perp z$ spin orientations $[E_i(||z)]$ and $E_i(\perp c)$, respectively obtained from DFT + U + SOC calculations. That is,

$$A_i \hat{S}_{iz}^2 = E_i(||z|) - E_i(\perp z) \tag{42}$$

so that $A_i < 0$ for easy-axis anisotropy, and $A_i > 0$ for easy-plane anisotropy. When a spin site has low symmetry, the description of its single-ion anisotropy requires more parameters to determine (see Appendix).

In the effective spin approximation, one circumvents the need to explicitly describe the unquenched orbital moments of a magnetic system by treating the system as a spin-only system. The effect of unquenched orbital moments is treated indirectly by introducing anisotropic g-factors. As a consequence, for a magnetic ion with nondegenerate magnetic orbitals (e.g., Cu^{2+}), the SOC Hamiltonian \hat{H}_{SO} is replaced with the zero-field spin Hamiltonian $\hat{H}_{
m zf}^{}$

$$\hat{H}_{zf} = D\hat{S}_{z}^{2} + E(\hat{S}_{x}^{2} - \hat{S}_{y}^{2}) - \frac{1}{3}D\hat{S}^{2}$$

$$= D\hat{S}_{z}^{2} + \frac{1}{2}E(\hat{S}_{+}\hat{S}_{+} + \hat{S}_{-}\hat{S}_{-}) - \frac{1}{3}D\hat{S}^{2}$$
(43)

where $D \propto \lambda^2(\delta L_{||} - \delta L_{\perp})$, where $\delta L_{||}$ and δL_{\perp} are the unquenched orbital angular momenta along the ||z| and $\perp z$ directions, respectively, and $E \propto \lambda^2 (\delta L_x - \delta L_y)$, where δL_x and δL_{ν} are the unquenched orbital angular momenta along the x- and y-directions, respectively. This line of reasoning might lead one to suggest that an S = 1/2 ion has no single-ion magnetic anisotropy.40 For the up-spin and down-spin states, $\alpha = \left| \frac{1}{2}, \frac{1}{2} \right\rangle$ and $\beta = \left| \frac{1}{2}, -\frac{1}{2} \right\rangle$, do not interact under \hat{H}_{zf} (namely, $\langle \alpha | \hat{H}_{zf} | \beta \rangle = 0$) so that, as dictated by the Kramers degeneracy theorem, the up-spin and down-spin states remain degenerate under SOC. However, one should note that this theorem says nothing about the preferred orientation of the α and β spins, but only about their degeneracy. Indeed, the neutron diffraction measurements for LiCuVO₄, 30 CuCl₂ 74 and CuBr₂, 75 which consist of CuL2 ribbon chains made up of edge-sharing CuL_4 square planes (L = O, Cl, Br), show that the Cu^{2+} (S = 1/2, d⁹) spins possess easy-plane anisotropy, that is, the spins prefer to lie in the plane of the $x^2 - y^2$ magnetic orbital in these compounds. Experimentally, it has been controversial whether the Cu²⁺ ion of Bi₂CuO₄ has easy-plane⁷⁶ or easyaxis⁷⁷ magnetic anisotropy. As mentioned in the previous section, DFT + U + SOC calculations for LiCuVO₄, Bi₂CuO₄, CuCl₂ and CuBr₂ predict the in-plane anisotropy for the Cu²⁺ ion, and our analysis shows why this should be the case. Thus, "no magnetic anisotropy for an S=1/2 magnetic ion" is inconsistent with experiment, DFT + U + SOC calculations and perturbation theory analysis.⁷²

C. Uniaxial magnetism vs. Jahn-Teller instability

Dalton Transactions

When a transition-metal magnetic ion is located at a coordination site with 3-fold or higher rotational symmetry, its dstates have doubly-degenerate levels, namely, (xz, yz) and (xy, yz) $(x^2 - y^2)$, if the z-axis is taken along the rotational axis. When such an ion has a more than half-filled d-shell, its d-electron configuration may lead to an unevenly-filled degenerate level, which leads to first-order Jahn-Teller instability. A representative example is found for the high-spin Fe^{2+} ($S = 2, d^6$) ion at the D_{3d} symmetry site in $(Me_3Si)_3C$ -Fe- $C(SiMe_3)_3$, in which the Fe²⁺ ion in the linear C-Fe-C coordination has the electron configuration $(xy, x^2 - y^2)^3(xz, yz)^2(z^2)^1$ (Fig. 10d).^{78,79} The latter has an unquenched orbital angular momentum of magnitude L=2 (in units of \hbar). Since the Fe²⁺ (S=2, L=2) ion has its d-shell more than half-filled, its SOC constant λ is negative so that, in its spin-orbit coupled states, the lowest-energy state arises from J = S + L = 4 and consists of the doublet described by $J_z = \pm 4.^{79}$ For convenience, the functions Φ_4 and Φ_{-4} may be used to represent this doublet.

To examine the magnetic moment associated with the above doublet Φ_4 and Φ_{-4} , we consider if the doublet is split in energy under magnetic field \vec{H} .⁷⁹ The Zeeman interaction under magnetic field is given by

$$\hat{H}_{\rm Z} = \mu_{\rm B}(\hat{L} + 2\hat{S}) \cdot \vec{H} \tag{44}$$

If we take the z-axis along the linear C-Fe-C direction, the Zeeman interaction for the field along the z-direction, $H_{||}$, is written as

$$\hat{H}_{z||} = \mu_{\rm B}(\hat{L}_{\rm z} + 2\hat{S}_{\rm z}) \cdot \hat{H}_{||}.$$
 (45a)

This Hamiltonian gives rise to a nonzero matrix element between two states with identical J_z values. The Zeeman interaction for the field perpendicular to the z-direction, H_\perp , is written as

$$\hat{H}_{Z\perp} = \mu_{\rm B} \left[\frac{1}{2} (\hat{L}_+ + \hat{L}_-) + (\hat{S}_+ + \hat{S}_-) \right] H_\perp, \tag{45b}$$

which leads to a nonzero matrix element between two states only if their J_z value difference $-J_z$ is equal to 1. For the field along the *z*-direction,

$$\langle \Phi_4 | \hat{H}_{z\parallel} | \Phi_4 \rangle = -\langle \Phi_{-4} | \hat{H}_{z\parallel} | \Phi_{-4} \rangle \neq \text{, and } \langle \Phi_{-4} | \hat{H}_{z\parallel} | \Phi_{-4} \rangle = 0$$

Thus, for $H_{||}$, the doublets are split in energy by

$$\Delta E_{\parallel} = 2\langle \Phi_4 | \hat{H}_{z\parallel} | \Phi_4 \rangle, \tag{46a}$$

so that there is a nonzero magnetic moment parallel to the *z*-direction. For the field perpendicular to the *z*-direction,

$$\langle \Phi_4 | \hat{H}_{z\perp} | \Phi_4 \rangle = -\langle \Phi_{-4} | \hat{H}_{z\perp} | \Phi_{-4} \rangle =$$
, and $\langle \Phi_{-4} | \hat{H}_{z\perp} | \Phi_{-4} \rangle = 0$

Thus, for H_{\perp} , the doublets Φ_4 and Φ_{-4} do not split so that the split energy $\Delta E_{||}$ is zero,

$$\Delta E_{||} = 0. \tag{47b}$$

Consequently, the magnetic moment is zero along all directions perpendicular to the *z*-axis and hence the linear C–Fe–C system with a high-spin Fe²⁺ ion is uniaxial. The g-factors for the parallel and perpendicular directions are then given by

$$g_{||} = \frac{\Delta E_{||}}{\mu_{\rm B} H_{||}} = \frac{2\langle \Phi_4 | \hat{L}_z + 2\hat{S}_z | \Phi_4 \rangle}{\mu_{\rm B} H_{||}} = 12$$
 (48a)

$$g_{\perp} = \frac{\Delta E_{\perp}}{\mu_{\rm B} H_{\perp}} = 0 \tag{48b}$$

A similar situation occurs for a high-spin Co^{2+} ($S = 3/2, d^7$) or Co^{3+} (S = 2, d^6) ion in a CoO_6 trigonal prism (Fig. 19a). ⁷⁹⁻⁸¹ A Co^{2+} (S = 3/2, d^{7}) ion at a trigonal prism site in $Ca_{3}CoRhO_{6}$ and $\text{Ca}_3\text{CoIrO}_6^{80,81}$ has the electron configuration $(z^2)^2(xy, x^2$ y^2)³(xz, yz)² (Fig. 19b) so that L = 2 and hence J = 7/2. Therefore, in the lowest-energy doublet state, $\Delta J_z = 7$ so that the high-spin Co²⁺ ion of a CoO₆ trigonal prism is uniaxial.⁸⁰ An interesting situation is presented by the high-spin Co^{3+} (S = 2, d^6) ion in each CoO₆ trigonal prism of Ca₃Co₂O₆. ⁷⁹⁻⁸¹ An isolated CoO₆ trigonal prism is expected to have the configuration $(z^2)^2(xy,$ $(x^2 - y^2)^2(xz, yz)^2$ with L = 0 (Fig. 19c), so it should not have uniaxial magnetism. Nevertheless, uniaxial magnetism is found for the high-spin Co^{3+} (S = 2, d^6) ions of the CoO_6 trigonal prisms in $Ca_3Co_2O_6$ as if its configuration is $(z^2)^1(xy, x^2 (y^2)^3(xz, yz)^2$ with L = 2 (Fig. 19d). 40,79,81 In understanding why this happens, one needs to consider the three different factors affecting the relative energies of the Co 3d states, as discussed below.

Ca₃Co₂O₆ consists of Co₂O₆ chains in which CoO₆ trigonal prisms alternate with CoO₆ octahedra by sharing their faces (Fig. 20a). For simplicity, trigonal prism and octahedral CoO₆

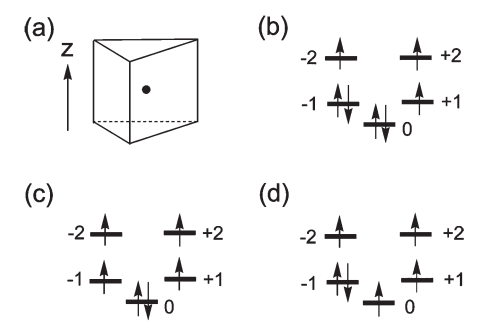


Fig. 19 (a) A CoO $_6$ trigonal prism found in Ca $_3$ CoMO $_6$ (M = Co, Rh, Ir). (b) The d-electron configuration of a high-spin Co $^{2+}$ (S=3/2, d^7) ion at a CoO $_6$ trigonal prism. (c) The d-electron configuration of a Co $^{3+}$ (S=2, d^6) ion at an isolated CoO $_6$ trigonal prism. (d) The d-electron configuration of a Co $^{3+}$ (S=2, d^6) ion at the CoO $_6$ trigonal prism of Ca $_3$ Co $_2$ O $_6$.

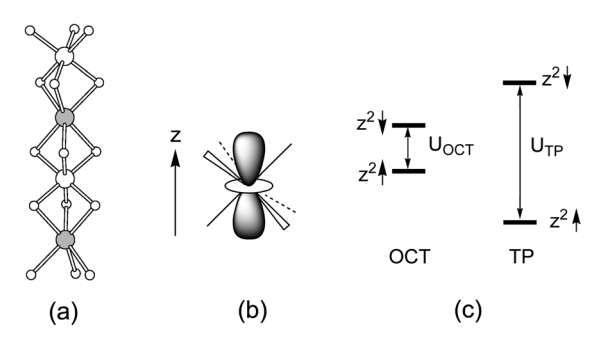


Fig. 20 (a) The CoMO₆ (M = Co, Rh, Ir) chain, made up of face sharing CoO₆ trigonal prisms and MO₆ octahedra, found in Ca₃CoMO₆. The Co atoms of the CoO_6 trigonal prisms are indicated by shaded cicles. (b) The z^2 orbital of an MO_6 octahedron. (c) The up-spin and down-spin z^2 orbitals at the octahedral and trigonal prism sites of a CoMO₆ (M = Co, Rh, Ir) chain.

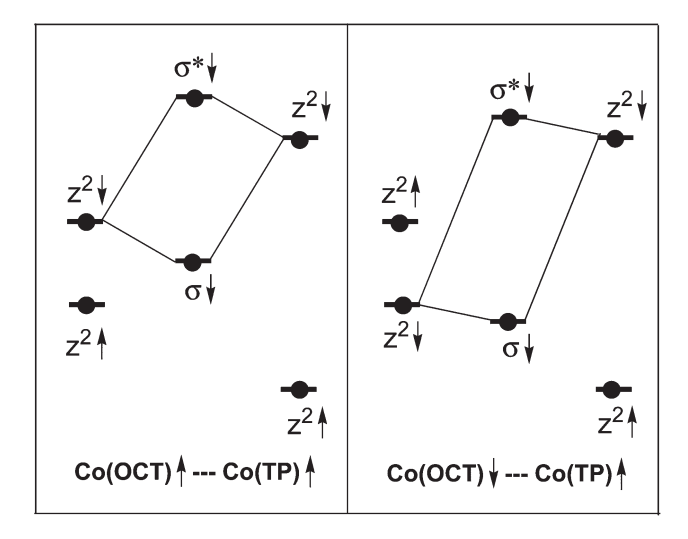
will be referred to as TP and OCT CoO6, respectively. Due to the face-sharing, the NN Co···Co distance in the Co₂O₆ chain is very short (2.595 Å). Ca₃Co₂O₆ shows that the TP Co³⁺ ion has the L = 2 configuration $(d_0)^1(d_2, d_{-2})^3(d_1, d_{-1})^2$ in the DFT + U + SOC calculations but the L = 0 configuration $(d_0)^2(d_2,$ $(d_{-2})^2(d_1, d_{-1})^2$ in the DFT + U calculations. 80,82 To understand the switching of the L=0 configuration to the L=2 configuration by the action of SOC, one needs to consider three effects, i.e., the spin arrangement between adjacent TP and OCT Co³⁺ ions, the direct metal-metal interaction between them, and the SOC on the TP Co3+ ion. It is convenient to discuss these factors by considering an isolated dimer made up of adjacent TP CoO6 and OCT CoO6. We first consider the interaction between the z^2 orbitals of adjacent Co^{3+} ions. In a one-electron tight-binding description, the high-spin Co³⁺ (d⁶) ion of an isolated TP CoO₆ has the $(d_0)^2(d_2, d_{-2})^2(d_1, d_{-1})^2$ configuration while the low-spin Co3+ (d6) ion of an isolated OCT CoO6 has the $(t_{2g})^6$ configuration. The OCT CoO₆ in Ca₃Co₂O₆ has C_3 symmetry, so the t_{2g} level is split into the 1a and 1e set. The z^2 orbital of the TP Co3+ ion can overlap strongly in a sigma fashion, and hence interacts strongly with the 1a orbital, i.e., the z^2 orbital (Fig. 20b), of the OCT Co^{3+} ion through the shared triangular face. In describing such an interaction at the spin-polarized DFT + U level, it should be noted that one-electron energy levels given by tight-binding calculations are split into the up-spin and down-spin levels by the spin-polarization/ on-site repulsion as depicted in Fig. 20c. 40,80 The $z^2 \uparrow$ and $z^2 \downarrow$ levels of the OCT Co3+ ion are split less than those of the TP Co³⁺ ion because, to a first approximation, the OCT site has a low-spin Co³⁺ ion whereas the TP site has a high-spin Co³⁺ ion. Since both TP and OCT sites have Co3+ ions, the midpoint between their $z^2 \uparrow$ and $z^2 \downarrow$ levels should be nearly the same. According to eqn (37), the L = 0 configuration of the TP Co^{3+} ion can be written as $(d_0)^2(d_2, d_{-2})^2(d_1, d_{-1})^2$ in a one-electron picture, which means in terms of spin polarized DFT + U calculations

$$\begin{split} \left(d_0\uparrow\right)^1 &< \left(d_2\uparrow, d_{-2}\uparrow\right)^2 < \left(d_1\uparrow, d_{-1}\uparrow\right)^2 < \left(d_0\downarrow\right)^1 \\ &< \left(d_2\downarrow, d_{-2}\downarrow\right)^0 < \left(d_1\downarrow, d_{-1}\downarrow\right)^0 \end{split}$$

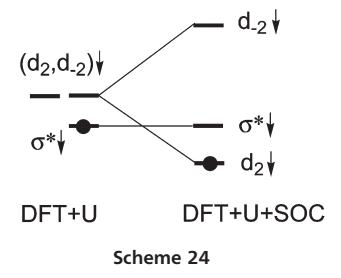
so the HOMO and LUMO of the TP CoO₆ are given by the d₀↓ and $(d_2\downarrow, d_{-2}\downarrow)$ levels, respectively. Therefore, if one of the four electrons present in the two z^2 orbitals of adjacent TP and OCT Co^{3+} ions is transferred to the $(d_2\downarrow, d_{-2}\downarrow)$ level of the TP Co^{3+} ion, the resulting electron configuration of the TP Co³⁺ ion would be close to $(d_0)^1(d_2,d_{-2})^3(d_1,d_{-1})^2$.

Consider that the spins of the TP and OCT Co³⁺ ions have the FM arrangement as indicated in Scheme 23 (left), as found experimentally. Here the closed circles refer to an occupied orbital. The highest occupied level resulting from the z^2 orbitals of the two Co^{3+} ions is the sigma antibonding level $\sigma^* \downarrow$, in which the weight of the trigonal-prism $z^2 \downarrow$ orbital is larger than that of the octahedral $z^2 \downarrow$ orbital because the former lies higher in energy than the latter. In the DFT + U level of description, the occupied $\sigma^*\downarrow$ level lies below the empty (d₂, d_{-2}) level of the TP Co³⁺ ion. If the TP and OCT Co³⁺ ions were to have the AFM arrangement as indicated in Scheme 23 (right), the resulting occupied $\sigma^*\downarrow$ level would be lower-lying compared with that resulting from the FM arrangement.

The effect of the SOC interaction at the TP Co³⁺ ion site is depicted in Scheme 24, where the SOC splits the unoccupied degenerate level $(d_2\downarrow, d_{-2}\downarrow)$ into the $d_2\downarrow$ below the $d_{-2}\downarrow$ pattern since $\lambda < 0$ for Co^{3+} (d^6). When the unoccupied $d_2 \downarrow$ level is lowered below the occupied $\sigma^*\downarrow$ level, an electron transfer occurs from the $\sigma^*\downarrow$ level to the $d_2\downarrow$ level. Since the $\sigma^*\downarrow$ level has a greater weight on the trigonal-prism $z^2 \downarrow$ orbital, this charge transfer effectively amounts to the configuration switch



Scheme 23



Dalton Transactions Perspective

of the TP Co^{3+} from the L=0 configuration $(d_0)^2(d_2, d_{-2})^2(d_1, d_{-2})^2$ $(d_{-1})^2$ to the L = 2 configuration $(d_0)^1(d_2, d_{-2})^3(d_1, d_{-1})^2$. This is why the TP Co^{3+} ion has the $(d_0)^2(d_2, d_{-2})^2(d_1, d_{-1})^2$ configuration at the DFT + U level, but has the $(d_0)^1(d_2, d_{-2})^3(d_1, d_{-1})^2$ configuration at the DFT + U + SOC level.

Note from Fig. 19 that the L = 2 electron configurations responsible for uniaxial magnetism induce a first-order Jahn-Teller distortion, 80,83 which removes the 3-fold rotational symmetry and hence lifts the degeneracies of (d_2, d_{-2}) and (d_1, d_2) d_{-1}). As a result, the orbital moment is strongly quenched. DFT + U + SOC calculations for Ca_3CoMO_6 (M = Co, Rh, Ir)⁸⁰ and Ca₃CoMnO₆ 83 show that the TP Co³⁺ ion of Ca₃Co₂O₆, the TP Co²⁺ ions of Ca₃CoRhO₆, Ca₃CoIrO₆ and Ca₃CoMnO₆ have the orbital moment of approximately 1.5 $\mu_{\rm B}$ in the absence of Jahn-Teller distortion but approximately 0.5 $\mu_{\rm B}$ in the presence of Jahn-Teller distortion. That is, the loss of the three-fold symmetry significantly quenches the orbital moment.

D. Singlet-triplet mixing and phosphorescence

Let us consider the singlet and triplet excited states, Ψ_{S} and $\Psi_{\rm T}$, respectively, resulting from a singlet ground state $\Psi_{\rm G}$. In the absence of SOC, the excited states Ψ_{S} and Ψ_{T} do not interact. In general, the spin parts of the singlet and triplet states are given by

$$|S\rangle = |s = 0, \ s_z = 0\rangle$$

 $|T\rangle = |s = 1, \ s_z = -1\rangle, \ |s = 1, \ s_z = 0\rangle, \ \text{or} \ |s = 1, \ s_z = 1\rangle$
(49)

Under SOC these two states interact because the interaction term $\langle T|\hat{H}_{SO}|S\rangle$ is nonzero. Namely, according to eqn (41b),

$$\langle T|\hat{H}_{SO}|S\rangle = \langle T|\hat{H}'_{SO}|S\rangle = \langle T|\hat{S}_{+'}|S\rangle \left(-\frac{\lambda}{2}\hat{L}_z\sin\theta\right).$$
 (50a)

Since the $\langle T|\hat{S}_{+'}|S\rangle$ term is nonzero, $\langle \Psi_{\rm T}|\hat{H}_{\rm SO}|\Psi_{\rm S}\rangle$ is nonzero,

$$\langle \Psi_{\rm T} | \hat{H}_{\rm SO} | \Psi_{\rm S} \rangle = \langle \Psi_{\rm T} | \hat{H}_{\rm SO}' | \Psi_{\rm S} \rangle^{\circ} \gamma, \tag{50b}$$

where γ represents a very small nonzero number. This means that under SOC the states $\Psi_{\rm S}$ and $\Psi_{\rm T}$ interact to generate mixed states,

$$\begin{aligned} \Psi'_{S} &\approx (1 - \gamma^{2}) \Psi_{S} + \gamma \Psi_{T} \\ \Psi'_{T} &\approx \gamma \Psi_{S} + (1 - \gamma^{2}) \Psi_{T} \end{aligned} \tag{51}$$

so that there exist no pure singlet and no pure triplet states once the effect of SOC is considered. Consequently, the transition dipole moment $\langle \Psi_{\rm G} | e \vec{r} | \Psi_{\rm T} \rangle$ between the ground singlet state Ψ_G and the "triplet" excited state Ψ_T is nonzero, because

$$\langle \Psi_{G} | e\vec{r} | \Psi_{T}' \rangle = \gamma \langle \Psi_{G} | e\vec{r} | \Psi_{S} \rangle \neq 0 \tag{52}$$

This explains why the transition from the "triplet" excited state Ψ_T to the singlet ground state Ψ_G (*i.e.*, phosphorescence) takes place, though very weakly. The forbiddnness of this transition is true only when the effect of SOC is neglected.

Dzyaloshinskii-Moriya interaction^{40,50}

A. Origin of DM interaction

Another important consequence of SOC is the DM interactions between two adjacent spin sites. Let us now examine the SOC in a spin dimer made up of two spin sites 1 and 2, for which the SOC Hamiltonian is given by⁴⁰

$$\hat{H}_{SO} = \lambda \hat{L} \cdot \hat{S} = \lambda (\hat{L}_1 + \hat{L}_2) \cdot (\hat{S}_1 + \hat{S}_2) \approx \lambda (\hat{L}_1 \cdot \hat{S}_1 + \hat{L}_2 \cdot \hat{S}_2)$$
 (53)

where the last equality follows from the fact that the SOC is a local interaction. It is important to note that, despite the local nature of SOC, the two spin sites can interact indirectly hence influencing their relative spin orientations. As illustrated in Scheme 25, we suppose that an occupied orbital ϕ_i interacts with an unoccupied orbital ϕ_i at spin site 1 *via* SOC, and that the ϕ_i and ϕ_i of site 1 interact with an occupied orbital ϕ_k of site 2 via orbital interaction. The orbital mixing between ϕ_i and ϕ_k introduces the spin character of site 2 into ϕ_i of site 1, while that between ϕ_i and ϕ_k introduces the spin character of site 2 into ϕ_i of site 1. Namely,

$$\phi_i \to \phi'_i \approx (1 - \gamma^2)\phi_i + \gamma \phi_k$$

$$\phi_i \to \phi'_i \approx (1 - \gamma^2)\phi_i + \gamma \phi_k$$

where γ refers to a small mixing coefficient. Then, the SOC between such modified ϕ'_i and ϕ'_i at site 1 indirectly introduces the interaction between the spins at sites 1 and 2. For a spin dimer, there can be a number of interactions like the one depicted in Scheme 25 at both spin sites, so summing up all such contributions gives rise to the DM interaction energy E_{DM} between spin sites 1 and 2.

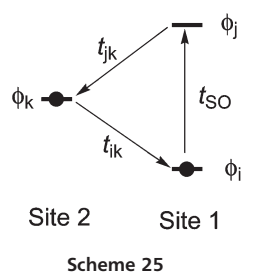
Suppose that $\delta \vec{L}_1$ and $\delta \vec{L}_2$ are the unquenched orbital angular momenta at sites 1 and 2, respectively. Then, use of the \hat{H}_{SO} (eqn (53)) as perturbation leads to the DM interaction energy $E_{\rm DM}$, 40,50

$$E_{\rm DM} = [\lambda J_{12}(\delta \vec{L}_1 - \delta \vec{L}_2)] \cdot (\vec{S}_1 \times \vec{S}_2) \equiv \vec{D}_{12} \cdot (\vec{S}_1 \times \vec{S}_2) \tag{54}$$

In this expression, the DM vector \vec{D}_{12} is related to the difference in the unquenched orbital angular momenta on the two magnetic sites 1 and 2, namely,

$$\vec{D}_{12} = \lambda J_{12} (\delta \vec{L}_1 - \delta \vec{L}_2). \tag{55}$$

For a spin dimer with Heisenberg exchange J_{12} , the strength of its DM exchange \vec{D}_{12} is discussed by considering the ratio $|D_{12}/J_{12}|$, which is often approximated by $|D_{12}/J_{12}| \approx \Delta g/g$,



This journal is © The Royal Society of Chemistry 2013

where Δg is the contribution of the orbital moment to the g-factor g in the effective spin approximation. In general, the $\Delta g/g$ value is at most 0.1, so that the $|D_{12}/J_{12}|$ ratio is often expected to be 0.1 at most. However, it is important to recognize an implicit assumption behind this reasoning, namely, that the spin sites 1 and 2 have an identical chemical environment. When the two spin sites have different chemical environments (see Fig. 15), the $|D_{12}/J_{12}|$ ratio can be very large as found for a particular Mn2³⁺-O-Mn3⁴⁺ spin exchange path of CaMn₇O₁₂ (*i.e.*, $|D_{12}/J_{12}| = 0.54$).^{55a} As depicted in Scheme 25, the magnitude of a DM vector D_{12} is determined by the three matrix elements, $t_{\rm SO} = \langle \phi_i | \hat{H}_{\rm SO} | \phi_j \rangle$, $t_{ik} = \langle \phi_i | \hat{H}^{\rm eff} |$ ϕ_k), and $t_{jk} = \langle \phi_j | \hat{H}^{\text{eff}} | \phi_k \rangle$. When t_{SO} , t_{ik} and t_{jk} are all strong, the magnitude of the DM vector D_{12} can be unusually large. We note that, in the multiferroic compound Cu₂OSeO₃, even the $|D_{12}/J_{12}|$ ratio greater than 1 (i.e., 1.95) is found for a particular interaction between two Cu2+ ions at different coordinate sites (i.e., trigonal bipyrimidal and square pyramidal sites).55b

B. Mapping analysis for the DM vector of an isolated spin dimer

Let us now consider how to determine the DM vector of an isolated spin dimer. So far, a spin dimer made up of spin sites 1 and 2 has been described by the spin Hamiltonian, $\hat{H}_{\rm spin}$ = $J_{12}\hat{S}_1\cdot\hat{S}_2$, composed of only a Heisenberg spin exchange. This Hamiltonian leads to a collinear spin arrangement (either FM of AFM), as already mentioned. To allow for a canting of the spins \vec{S}_1 and \vec{S}_2 from the collinear arrangement (typically from the AFM arrangement), it is necessary to include the DM exchange $\vec{D}_{12} \cdot (\hat{S}_1 \times \hat{S}_2)$ into the spin Hamiltonian. That is,

$$\hat{H}_{\text{spin}} = J_{12}\hat{S}_1 \cdot \hat{S}_2 + \vec{D}_{12} \cdot (\hat{S}_1 \times \hat{S}_2). \tag{56}$$

The $\hat{S}_1 \times \hat{S}_2$ term, being proportional to $\sin \theta$ where θ is the angle between the two spin vectors \vec{S}_1 and \vec{S}_2 , is nonzero only if the two spins are not collinear. Thus, the DM interaction $\vec{D}_{12} \cdot (\hat{S}_1 \times \hat{S}_2)$ induces spin canting. (Of course, even if a model Hamiltonian consists of only Heisenberg spin exchanges, a magnetic system with more than two spin sites can have a non-collinear spin arrangement if there exists spin frustration (Section 6A).)

As discussed in Section 4A, the Heisenberg exchange J_{12} of eqn (56) can be evaluated on the basis of energy-mapping analysis by considering two collinear spin states |HS\rangle and |BS\rangle (i.e., FM and AFM spin arrangements, respectively) because the DM exchange $\vec{D}_{12} \cdot (\hat{S}_1 \times \hat{S}_2)$ is zero for such collinear spin states. To evaluate the DM vector \vec{D}_{12} , we carry out energymapping analysis on the basis of DFT + U + SOC calculations.²³ In terms of its Cartesian components, \vec{D}_{12} is expressed as

$$\vec{D}_{12} = \hat{i}D_{12}^x + \hat{j}D_{12}^y + \hat{k}D_{12}^z$$

Therefore, the DM interaction energy $\vec{D}_{12} \cdot (\hat{S}_1 \times \hat{S}_2)$ is rewritten as

$$\vec{D}_{12} \cdot (\hat{S}_{1} \times \hat{S}_{2}) = (\hat{i}D_{12}^{x} + \hat{j}D_{12}^{y} + \hat{k}D_{12}^{z}) \cdot \begin{pmatrix} \hat{i} & \hat{j} & \hat{k} \\ \hat{S}_{1}^{x} & \hat{S}_{1}^{y} & \hat{S}_{1}^{z} \\ \hat{S}_{2}^{x} & \hat{S}_{2}^{y} & \hat{S}_{2}^{z} \end{pmatrix}$$

$$= D_{12}^{x}(\hat{S}_{1}^{y}\hat{S}_{2}^{z} - \hat{S}_{1}^{z}\hat{S}_{2}^{y}) - D_{12}^{y}(\hat{S}_{1}^{x}\hat{S}_{2}^{z} - \hat{S}_{1}^{z}\hat{S}_{2}^{x})$$

$$+ D_{12}^{z}(\hat{S}_{1}^{x}\hat{S}_{2}^{y} - \hat{S}_{1}^{y}\hat{S}_{2}^{x})$$

$$+ D_{12}^{z}(\hat{S}_{1}^{x}\hat{S}_{2}^{y} - \hat{S}_{1}^{y}\hat{S}_{2}^{x})$$

$$(57)$$

To determine the D_{12}^z component, we consider the following two orthogonally ordered spin states,

State 1:
$$\vec{S}_1 = (S, 0, 0)$$
 and $\vec{S}_2 = (0, S, 0)$

State 2:
$$\vec{S}_1 = (S, 0, 0)$$
 and $\vec{S}_2 = (0, -S, 0)$

where S is the length of the spin. In state 1, the spins at sites 1 and 2 are along the positive x and the positive y directions, respectively. In state 2, the spins at sites 1 and 2 are along the positive x and the negative y directions, respectively. For these states, $\vec{S}_1 \cdot \vec{S}_2 = 0$ and $|\vec{S}_1 \times \vec{S}_2| = S^2$ so that, according to eqn (57), the energies of the two states are given by $E_1 = S^2 D_{12}^z$ and $E_2 = S^2 D_{12}^z$. Consequently,

$$D_{12}^{z} = \frac{1}{2}(E_1 - E_2)/S^2.$$
 (58a)

Thus, D_{12}^z is determined by evaluating the energies E_1 and E_2 on the basis of DFT + U + SOC calculations.

The D_{12}^y and D_{12}^x components are determined in a similar manner. Using the following two orthogonal spin states,

State 3:
$$\vec{S}_1 = (S, 0, 0)$$
 and $\vec{S}_2 = (0, 0, -S)$

State 4:
$$\vec{S}_1 = (S, 0, 0)$$
 and $\vec{S}_2 = (0, 0, S)$

the D_{12}^{y} component is obtained as

$$D_{12}^{y} = \frac{1}{2}(E_3 - E_4)/S^2 \tag{58b}$$

In terms of the following two orthogonal spin states,

State 5:
$$\vec{S}_1 = (0, S, 0)$$
 and $\vec{S}_2 = (0, 0, S)$

State 6:
$$\vec{S}_1 = (0, S, 0)$$
 and $\vec{S}_2 = (0, 0, -S)$

the D_{12}^x term is given by

$$D_{12}^{x} = \frac{1}{2}(E_5 - E_6)/S^2$$
 (58c)

C. Mapping analysis for the DM vectors of a general magnetic solid²³

For a given pair of spins in a general magnetic solid, the D_{12}^x , D_{12}^{y} and D_{12}^{z} components can be similarly extracted by performing DFT + U + SOC calculations for four non-collinearly ordered spin states in which all spin exchange interactions associated with the spin sites 1 and 2 vanish.²³ In such a case the relative energies of the four states are related only to the energy differences in their DM interactions (see Appendix).

Dalton Transactions Perspective

10. Interaction between transition-metal and rare-earth ions⁸⁴

A. Spin reorientation in a square-lattice antiferromagnet

Exchange interactions between transition-metal (TM) and rareearth (RE) ions have been less extensively studied than those between TM ions. We now examine the exchange interactions between RE and TM ions in the square-lattice antiferromagnet CeMnAsO (Fig. 21a), 85,86 in which each square sheet of highspin Mn^{2+} (d^5 , S = 5/2) ions is sandwiched between two square sheets of As³⁻ ions to form an As-Mn-As slab. This As-Mn-As slab is made up of edge-sharing MnAs₄ tetrahedra. Similarly, each square sheet of O2- ions is sandwiched between two square sheets of Ce3+ (f1) ions to form a Ce-O-Ce slab. This Ce-O-Ce slab is made up of edge-sharing OCe4 tetrahedra. In CeMnAsO the As-Mn-As slabs alternate with the Ce-O-Ce slabs along the c-direction such that each Ce is located above the center of an As4 square, and each As above the center of a Ce₄ square. Thus, the Ce³⁺ ions above and below the square sheet of the Mn²⁺ ions occupy the positions of neighboring Mn₄ squares, such that each Ce atom forms a Mn₄Ce square pyramid (Fig. 21b).

The Mn²⁺ (d⁵) ions in the square lattice of CeMnAsO undergo an AFM ordering at high temperatures ($T_N = 360 \text{ K}$) with the Mn moments oriented along the c-axis. CeMnAsO undergoes a spin-reorientation (SR) transition at low temperatures (T_{SR} = 34 K), below which the Mn moments rotate into the ab-plane. 85,86 Simultaneously, the Ce moments occur in the ab-plane with FM coupling in each sheet of Ce atoms parallel to the ab-plane, and two such sheets straddling each sheet of the Mn atoms have their moments antiferromagnetically coupled (e.g., Fig. 22).85,86 LaMnAsO is isostructural with CeMnAsO, but has no magnetic moment on La3+. LaMnAsO exhibits an AFM ordering of the Mn moments similar to that found for CeMnAsO between T_{SR} and T_{N} , but does not undergo a SR of the Mn moments.⁸⁷ This indicates that the SR in CeMnAsO is caused by the interaction between the Ce³⁺ and Mn²⁺ moments.

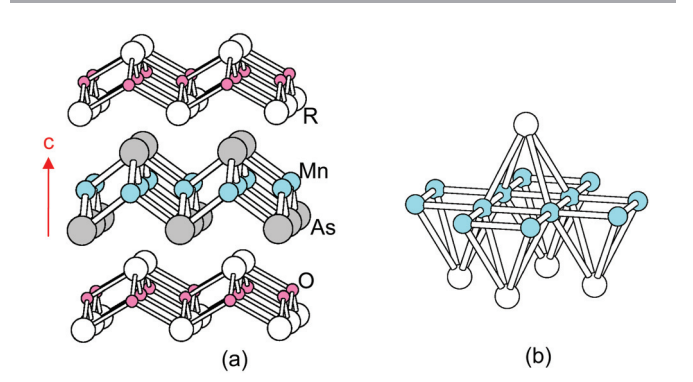


Fig. 21 (a) A perspective view of CeMnAsO, in which layers of CeO alternate with layers of MnAs. (b) A perspective view of the arrangement of the Ce³⁺ and Mn²⁺ ions in CeMnAsO, in which each Mn₄ square is capped by a Ce to form a Mn₄Ce square pyramid.

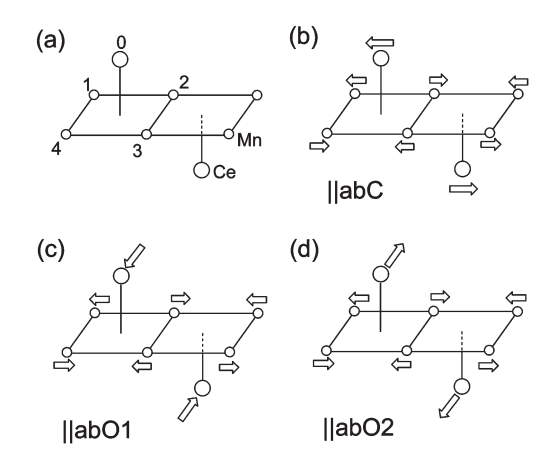


Fig. 22 (a) Two edge-sharing Mn₄Ce square pyramids in CeMnAsO. (b) The ||abC spin arrangement of the Mn²⁺ and Ce³⁺ moments. (c) The ||abO1 spin arrangement of the Mn^{2+} and Ce^{3+} moments. (d) The ||abO2 spin arrangement of the Mn²⁺ and Ce³⁺ moments. In (b), (c) and (d), the Mn²⁺ and Ce³⁺ moments are parallel to the ab-plane.

B. Competition between DM and biquadratic interactions

For convenience, in each Mn₄R square pyramid of RMnAsO, we label the R^{3+} ion as 0, and the Mn^{2+} ions as i (= 1-4) (Fig. 22a). In principle, the ordered R³⁺ and Mn²⁺ moments of RMnAsO below T_{SR} can be collinear (Fig. 22b) or orthogonal (Fig. 22b or 22c). The DM interaction between the R3+ and Mn²⁺ moments in RMnAsO is enhanced if the spins at these sites are large because it can increase the length of the vector $\vec{S}_0 \times \vec{S}_i$ (i = 1-4) thereby favoring an orthogonal arrangement of the R3+ and Mn2+ moments. However, this condition also enhances the contribution of the biquadratic (BQ) exchange $K_{ij}(\vec{S}_0 \cdot \vec{S}_i)^{2}$ 85,88 to the spin Hamiltonian,

$$\hat{H}_{\text{spin}} = \sum_{i < j} J_{ij} \hat{S}_i \cdot \hat{S}_j + \sum_{i < j} K_{ij} (\hat{S}_0 \cdot \hat{S}_i)^2$$

$$+ \sum_{i < j} \vec{D}_{ij} \cdot (\hat{S}_i \times \hat{S}_j)$$
(59)

where K_{ij} is the BQ exchange constant. The BQ exchange, which has often been neglected, favors a collinear spin arrangement. It is an important issue to know whether the DM or the BQ exchange dominates. (The single-ion anisotropy of the rare-earth ion was not included in eqn (59) because it is not crucial for the present system.85)

The relative energies of the collinear and orthogonal spin arrangements (ab||C, ab||O1 and ab||O2 in Fig. 22) of CeMnAsO may now be analyzed in terms of the spin Hamiltonian, eqn (59). The net Heisenberg exchange between the Ce^{3+} and Mn^{2+} ions is zero for the ||abC arrangement due to their spin frustration, and also for the ab||O1 and ab||O2arrangements due to their orthogonal spin arrangements. For the ab||C arrangement, the DM exchange energy (E_{DM}) is zero but the BQ exchange energy (E_{BO}) is not, because the Ce^{3+} and Mn^{2+} moments are collinear. For the $||ab\mathrm{O}1|$ and $||ab\mathrm{O}2|$ arrangements, $E_{BQ} = 0$ because the Ce^{3+} and Mn^{2+} moments are orthogonal, and their E_{DM} energies are nonzero and are

opposite in sign. Therefore,

$$2|E_{DM}| = |E(||abO1) - E(||abO2)|.$$
 (60a)

Let us use the notation $||abO_1|$ to indicate the lower-energy one of the ||abO1| and ||abO2| arrangements. Then the energy difference between the ||abC| and $||abO_1|$ states has both the BQ and the DM contributions. Thus,

$$E_{BQ} = E(||abC) - E(||abO_1) - |E_{DM}|$$
 (60b)

Our DFT + U + SOC calculations for the ||abC, ||abO1| and ||abO2| states of CeMnAsO show that the ||abO1| state is the lowest in energy, and $E_{\rm DM}$ = -4.88 meV and $E_{\rm BO}$ = -0.07 meV per formula unit (FU) of CeMnAsO.85 Thus, the orthogonal spin arrangement in CeMnAsO below the $T_{\rm SR}$ is caused by the DM interaction. NdMnAsO consists of Nd³⁺ (f³) and Mn²⁺ (d⁵) ions, is isostructural with CeMnAsO, and undergoes a SR $(T_{SR} = 23 \text{ K})^{87,89}$ as found for CeMnAsO. However, the Nd³⁺ and Mn^{2^+} moments are collinear in NdMnAsO below $T_{\mathrm{SR}}.^{87}$ In agreement with this finding, DFT + U + SOC calculations for NdMnAsO show that the ||abC| state is the lowest in energy, and $E_{\rm DM}$ = -0.35 meV/FU and $E_{\rm BQ}$ = -18.05 meV/FU.⁸⁵ Namely, the collinear spin arrangement in NdMnAsO below T_{SR} is caused by the BQ interaction. It is noteworthy that the DM interaction dominates over the BQ interaction in CeMnAsO, while the opposite is the case in NdMnAsO.

C. Qualitative aspects of DM exchanges between RE and TM ions⁸⁵

It is of interest to examine why the DM exchange is strong in CeMnAsO but weak in NdMnAsO. The DM exchange for each pair of Mn²⁺ and Ce³⁺ ions in a Mn₄Ce square pyramid (Fig. 22a, where the indices 0 and i refer to the RE and TM ions, respectively) is written as $\vec{D}_{0i} \cdot (\hat{S}_0 \times \hat{S}_i)$ (i = 1-4) with the DM vector expressed as $\vec{D}_{0i} = \sqrt{\lambda_0 \lambda_i} J_{0i} (\delta \vec{L}_0 - \delta \vec{L}_i)$, where λ_0 and λ_i are the SOC constants of the magnetic ions at 0 and i, respectively, while $\delta \vec{L}_0$ and $\delta \vec{L}_i$ are essentially the unquenched orbital momenta of the magnetic ions at 0 and i, respectively. For the S = 5/2 TM ion Mn²⁺, L = 0 to a first approximation so that $\delta \vec{L}_i \approx 0$. The f-orbitals of an R^{3+} ion overlap poorly with the orbitals of its surrounding ligands so that its spherical electron density distribution is weakly distorted by the surrounding ligands. Consequently, for a RE ion, the quenching of the orbital angular momentum is generally weak so that its $\delta \vec{L}_0$ can be large. Therefore, the DM vector for the exchange between such TM and RE ions can be approximated by

$$\vec{D}_{0i} = \sqrt{\lambda_0 \lambda_i} J_{0i} (\delta \vec{L}_0 - \delta \vec{L}_i) \approx \sqrt{\lambda_0 \lambda_i} J_{0i} \delta \vec{L}_0$$
 (61)

Consider the DM interaction around one Ce^{3+} ion of CeMnAsO in the ||abO1| arrangement (Fig. 22c). Then the E_{DM} is

expressed as

$$E_{\rm DM} = \vec{D}_{01} \cdot (\hat{S}_0 \times \hat{S}_1) + \vec{D}_{02} \cdot (\hat{S}_0 \times \hat{S}_2) + \vec{D}_{03} \cdot (\hat{S}_0 \times \hat{S}_3) + \vec{D}_{04} \cdot (\hat{S}_0 \times \hat{S}_4) = (\vec{D}_{01} - \vec{D}_{02} + \vec{D}_{03} - \vec{D}_{04}) \cdot (\hat{S}_0 \times \hat{S}_1)$$
(62)

Eqn (61) shows that the symmetry of the DM vectors \vec{D}_{0i} (i=1–4) is determined largely by that of the unquenched orbital momentum $\delta \vec{L}_0$ of the Ce³⁺ ion, namely, by the symmetry of the occupied 4f orbitals of the Ce³⁺ ion. DFT + U + SOC calculations for CeMnAsO show that the occupied 4f-states of the Ce³⁺ ion have only the $l_z=\pm 2$ orbital contributions.⁸⁵ In Cartesian coordinates, the ($l_z=\pm 2$, $l_z=-2$) orbitals correspond to the $\{f_{xyz}, f_{z(x^2-y^2)}\}$ orbitals, which switch their sign when rotated around the z-axis by every 90°. This means that $\vec{D}_{03}=\vec{D}_{03}=-\vec{D}_{02}=-\vec{D}_{04}$, so that

$$E_{\rm DM} = 4\vec{D}_{01} \cdot (\hat{S}_0 \times \hat{S}_1). \tag{63}$$

For the ||abO2| arrangement (Fig. 22d), $E_{\rm DM}=-4\vec{D}_{01}\cdot(\hat{S}_0\times\hat{S}_1)$ by symmetry.

DFT + U + SOC calculations for NdMnAsO show that the occupied 4f-states of the Nd³+ ion have a strong contribution from the $l_z=\pm 1$ orbitals, but weak contributions from the $l_z=\pm 2$ and $l_z=\pm 3$ orbitals. The $(l_z=+1,\ l_z=-1)$ orbitals correspond to the $\{f_{x(4z^2-x^2-y^2)},\ f_{y(4z^2-x^2-y^2)}\}$ orbitals in Cartesian coordinates, which switch their sign when rotated around the z-axis by 180° so that $\vec{D}_{01}=-\vec{D}_{03}$ and $\vec{D}_{02}=-\vec{D}_{04}$. Consequently, the DM exchange associated with these orbitals is zero, which makes the DM exchange small for NdMnAsO.

D. Model Hamiltonians beyond the level of spin exchange

In most cases a model Hamiltonian including only spin exchange interactions is adequate in describing magnetic systems.

$$\hat{H}_{\rm spin} = \sum_{i < j} J_{ij} \hat{S}_i \cdot \hat{S}_j \tag{21a}$$

When such a model Hamiltonian is not adequate enough, one might improve the model Hamiltonian by adding other energy terms. For example,

$$\hat{H}_{\text{spin}} = \sum_{i < j} J_{ij} \hat{S}_i \cdot \hat{S}_j + \sum_{i < j} \vec{D}_{ij} \cdot (\hat{S}_i \times \hat{S}_j). \tag{64a}$$

This spin Hamiltonian depends only on the relative orientations of the two spins. To describe the effect of absolute spin orientations on magnetic properties, one may introduce the single-ion anisotropy (or magnetocrystalline anisotropy) energy term $A_i \hat{S}_{iz}^2$ for each magnetic ion into the spin Hamiltonian. Then, the model Hamiltonian can be rewritten as

$$\hat{H}_{\text{spin}} = \sum_{i < j} J_{ij} \hat{S}_i \cdot \hat{S}_j + \sum_{i < j} \vec{D}_{ij} \cdot (\hat{S}_i \times \hat{S}_j) + \sum_i A_i S_{iz}^2. \quad (64b)$$

In discussing the interactions between RE and TM magnetic ions, even BQ spin exchange terms $K_{ij}(\hat{S}_i \cdot \hat{S}_j)^2$ are necessary, 85

Dalton Transactions Perspective

which leads to the model Hamiltonian

$$\hat{H}_{\text{spin}} = \sum_{i < j} J_{ij} \hat{S}_i \cdot \hat{S}_j + \sum_{i < j} K_{ij} (\hat{S}_i \cdot \hat{S}_j)^2$$

$$+ \sum_{i < j} \vec{D}_{ij} \cdot (\hat{S}_i \times \hat{S}_j) + \sum_{i} A_i S_{iz}^2$$
(64c)

Thus, depending on the nature of the magnetic properties to describe, the model Hamiltonian can become quite complex. In most cases, however, it is unnecessary and undesirable to have all the four terms in a spin Hamiltonian because the purpose of using a model Hamiltonian is to capture the essence of observed magnetic phenomena with a minimal set of parameters.

11. Concluding remarks

We surveyed various concepts and phenomena concerning magnetic properties from the perspective of electronic structure. Exchange interactions between magnetic ions are weak so that the energy levels of a magnetic system are closely packed. Thus, a succinct description of the associated magnetic properties requires the use of a model Hamiltonian defined in terms of Heisenberg (or symmetric) exchange, which may have to be supplemented by adding other weaker energy terms such as DM (or antisymmetric) exchange, BQ exchange and/or single-ion magnetic anisotropy. The signs and values of the constants specifying these terms can be determined on the basis of energy mapping analysis, in which the energy spectrum of a magnetic system determined from DFT electronic structure calculations for a set of broken-symmetry states is mapped onto that determined by a model Hamiltonian defined in terms of parameters to determine.

Though not discussed in this review, the literature on magnetic studies shows many examples in which the magnetic properties of a system were interpreted by using a spin lattice irrelevant for the system [*e.g.*, $Cu_3(P_2O_6OH)_2$, ⁶² $Cu_3(CO_3)_2(OH)_2$, ⁶⁴ $Cu_3(OH)_4SO_4$, ⁹⁰ Na_3RuO_4 , ⁹¹ $Bi_4Cu_3V_2O_{14}$, ⁹² $Na_3Cu_2SbO_6$ and $Na_2Cu_2TeO_6$, $Na_3Cu_2SbO_6$ and $Na_3Cu_2SbO_$ situations occur because a spin lattice is selected on the basis of the geometrical pattern of its magnetic ion arrangements and also by preferring, when the geometrical pattern suggests several spin lattices, the one that can generate a more interesting physics. It is important to realize that both M-L-M and M-L···L-M spin exchanges give rise to the magnetic bonds determining a spin lattice. The M-L···L-M exchanges, though frequently neglected, are often stronger than the M-L-M exchanges because the strength of a spin exchange is governed by how well the tails of the magnetic orbitals interact. It is essential that a spin lattice be selected on the basis of electronic structure considerations.

SOC plays an important role in determining magnetic properties. The spin orientation of a transition-metal magnetic ion is readily explained in terms of perturbation theory by considering its split d-block levels as unperturbed states and the SOC Hamiltonian $\hat{H}_{\rm SO}$ as perturbation. The DM interaction between adjacent spin sites occurs due to a consequence of SOC at

each spin site and the orbital interaction between the two spin sites. Given J as the Heisenberg exchange of the spin exchange path, the strength of the associated DM exchange D is frequently estimated by $|D/J| \approx \Delta g/g$, which is smaller than ~0.1. This estimate is valid only when the two spin sites have an identical chemical environment. When the two spin sites are not chemically equivalent, the |D/J| ratio can become very large because all three hopping processes leading to DM interaction can become large. For the DM interaction between RE and TM cations, the symmetry and strength of the DM vector are governed largely by the magnetic orbitals (i.e., singly occupied f orbitals) of the RE cation, because the f-orbitals of a RE cation overlap poorly with the orbitals of its surrounding ligands so that its spherical electron density distribution is weakly distorted by the surrounding ligands, and hence the quenching of its orbital angular momentum is weak. In the interaction between RE and TM cations, the DM and BQ exchanges compete such that their spins have an orthogonal arrangement when the DM exchange dominates, but a collinear spin arrangement if the BQ exchange dominates. It is an important issue to understand what factors govern the relative strengths of the DM and BQ exchanges.

Appendix: Energy-mapping analysis based on four ordered spin states

The spin Hamiltonian can be written as

$$\begin{split} \hat{H}_{\text{spin}} &= \sum\nolimits_{i < j} J_{ij} \vec{S}_i \cdot \vec{S}_j + \sum\nolimits_{i < j} \vec{D}_{ij} \cdot (\vec{S}_i \times \vec{S}_j) \\ &+ \sum\nolimits_{i,\alpha\beta} A_{i,\alpha\beta} \vec{S}_{i\alpha} \vec{S}_{i\beta} \end{split} \tag{A1}$$

where $J_{ij} = J_{ji}$, $\vec{D}_{ij} = -\vec{D}_{ji}$, $A_{i,\alpha\beta} = A_{i,\beta\alpha}$, and α , $\beta = x$, y, z. Let us define the following effective parameters:

$$J^{\rm e}_{ij}=S_iS_jJ_{ij}, \vec{D}^{\rm e}_{ij}=S_iS_j\vec{D}_{ij}, \text{ and } A^{\rm e}_{i,\alpha\beta}=S^2_iA_{i,\alpha\beta}. \tag{A2} \label{eq:A2}$$

Then, the spin vectors \vec{S}_i and \vec{S}_j of $\hat{H}_{\rm spin}$ become unit vectors. In the following, this will be assumed to be the case. Without loss of generality, the spin pair ij will be regarded as 12.

A. Heisenberg spin exchange²³

We carry out DFT + U calculations for the following four ordered spin states: where the notations (0, 0, 1) and (0, 0, -1), for example, mean that the unit vectors are pointed along the positive and negative *z*-directions, respectively. Then we obtain

$$J_{12}^{e} = \frac{E_1 + E_4 - E_2 - E_3}{4} \tag{A3}$$

State	Spin 1	Spin 2	Other spin sites
1	(0, 0, 1)	(0, 0, 1)	Either $(0, 0, 1)$ or $(0, 0, -1)$ according
2	(0, 0, 1)	(0, 0, -1)	to the experimental (or a low-energy)
3	(0, 0, -1)	(0, 0, 1)	spin state. Keep the same for the four
4	(0, 0, -1)	(0, 0, -1)	spin states

B. DM spin exchange²³

To calculate the z-component of D_{12}^{e} (i.e., $D_{12,z}^{e}$), we carry out DFT + U + SOC calculations for the following four ordered spin states:

Spin 1 Spin 2 Other spin sites (1, 0, 0)(0, 1, 0)Either (0, 0, 1) or (0, 0, -1) according to 1 2. (1, 0, 0)(0, -1, 0)the experimental (or a low-energy) spin 3 (-1, 0, 0)(0, 1, 0)state. Keep the same for the four spin (-1, 0, 0)(0, -1, 0)states

Then, we obtain

$$D_{12,z}^{e} = \frac{(E_1 + E_4) - (E_2 + E_3)}{4} \tag{A4}$$

To determine the y-component of D_{12}^{e} (i.e., $D_{12,y}^{e}$), we perform DFT + U + SOC calculations for the following four ordered spin states:

State Spin 1 Spin 2 Other spin sites (0, 0, 1)Either (0, 1, 0) or (0, -1, 0) according to (1, 0, 0)(1, 0, 0)(0, 0, -1)2. the experimental (or a low-energy) spin 3 state. Keep the same for the four spin (-1, 0, 0)(0, 0, 1)(-1, 0, 0)(0, 0, -1)states

Then,

$$D_{12,y}^{e} = \frac{-(E_1 + E_4) + (E_2 + E_3)}{4} \tag{A5}$$

To determine the x-component of D_{12}^{e} (i.e., $D_{12,x}^{e}$), we carry out DFT + U + SOC calculations for the following four ordered spin states:

Spin 2 State Spin 1 Other spin sites Either (1, 0, 0) or (-1, 0, 0) according to (0, 1, 0)(0, 0, 1)the experimental (or a low-energy) spin 2 (0, 1, 0)(0, 0, -1)3 (0, -1, 0)(0, 0, 1)state. Keep the same for the four spin (0, -1, 0)(0, 0, -1)states

Then,

$$D_{12,x}^{e} = \frac{(E_1 + E_4) - (E_2 + E_3)}{4} \tag{A6}$$

C. Single-ion anisotropy

For a given ion i, the most general form of the Hamiltonian \hat{H}_{SIA} describing the single-ion anisotropy (SIA) can be written as

$$\begin{split} \hat{H}_{\text{SIA}} &= A_{i,xx}^{e} S_{x}^{2} + A_{i,yy}^{e} S_{y}^{2} + A_{i,zz}^{e} S_{z}^{2} + 2 A_{i,xy}^{e} S_{x} S_{y} + 2 A_{i,xz}^{e} S_{x} S_{z} \\ &+ 2 A_{i,yz}^{e} S_{y} S_{z} \end{split} \tag{A7}$$

(a) If the ion has easy-axis or easy-plane anisotropy, the above Hamiltonian can be simplified as

$$\hat{H}_{SIA} = A_i^e S_{iz}^2 \tag{A8}$$

To determine A_i^e , we carry out DFT + U + SOC calculations for the following four ordered spin states:

State	Spin i	Other spin sites
1	(0, 0, 1)	Either $(0, 1, 0)$ or $(0, -1, 0)$ according to the
2	(0, 0, -1)	experimental (or a low-energy) spin state.
3	(1, 0, 0)	Keep the same for the four spin states
4	(-1, 0, 0)	

Then,

$$A_i^{\rm e} = \frac{(E_1 + E_2) - (E_3 + E_4)}{2} \tag{A9}$$

(b) If the ion site has low symmetry, all coefficients of eqn (A7) should be evaluated. We note the following relationship,

$$A_{i,xx}^{e}S_{x}^{2} + A_{i,yy}^{e}S_{y}^{2} + A_{i,zz}^{e}S_{z}^{2} = (A_{i,xx}^{e} + (A_{i,yy}^{e} - A_{i,xx}^{e})S_{y}^{2} + (A_{i,zz}^{e} - A_{i,xx}^{e})S_{z}^{2}$$
(A10)

Consequently, we need to determine only the five coefficients from DFT + U + SOC calculations as shown below.

(1) For $A_{i,xy}^e$:

$$A_{i,xy}^{e} = \frac{(E_1 + E_4) - (E_2 + E_3)}{4} \tag{A11}$$

State Spin i Other spin sites $(\sqrt{2}/2, \sqrt{2}/2, 0)$ Either (0, 0, 1) or (0, 0, -1) according to $(\sqrt{2}/2, -\sqrt{2}/2, 0)$ the experimental (or a low-energy) spin $(-\sqrt{2}/2, \sqrt{2}/2, 0)$ 3 state. Keep the same for the four spin $(-\sqrt{2}/2, -\sqrt{2}/2, 0)$

(2) For $A_{i,rz}^e$:

$$A_{i,xz}^{e} = \frac{(E_1 + E_4) - (E_2 + E_3)}{4}$$
 (A12)

Spin i State Other spin sites $(\sqrt{2}/2, 0, \sqrt{2}/2)$ Either (0, 1,0) or (0, -1, 0) according to $(\sqrt{2}/2, 0, -\sqrt{2}/2)$ the experimental (or a low-energy) spin $(-\sqrt{2}/2,0,\sqrt{2}/2)$ 3 state. Keep the same for the four spin 4 $(-\sqrt{2}/2, 0, -\sqrt{2}/2)$ states

(3) For $A_{i,xy}^e$:

$$A_{i,xy}^{e} = \frac{(E_1 + E_4) - (E_2 + E_3)}{4}$$
 (A13)

Spin i Other spin sites State $(0,\sqrt{2}/2,\sqrt{2}/2)$ Either (1, 0, 0) or (-1, 0, 0) according to $(0, \sqrt{2}/2, -\sqrt{2}/2)$ the experimental (or a low-energy) spin $\begin{array}{c} (0, -\sqrt{2}/2, \sqrt{2}/2) \\ (0, -\sqrt{2}/2, -\sqrt{2}/2) \end{array}$ state. Keep the same for the four spin

(4) For $(A_{i,yy}^{e} - A_{i,xx}^{e})$:

$$A_{i,yy}^{e} - A_{i,xx}^{e} = \frac{(E_1 + E_2) - (E_3 + E_4)}{2}$$
 (A14)

Spin i Other spin sites Either (0, 0, 1) or (0, 0, -1) according to the (0, 1, 0)experimental (or a low-energy) spin state. Keep the same for the four spin states

2 (0,-1,0)(1, 0, 0)(-1, 0, 0)

(5) For $(A_{i,zz}^{e} - A_{i,xx}^{e})$:

$$A_{i,xx}^{e} - A_{i,xx}^{e} = \frac{(E_1 + E_2) - (E_3 + E_4)}{2}$$
 (A15)

State Spin i Other spin sites 1 (0,0,1) Either (0,1,0) or (0,-1,0) according to 2 (0,0,-1) the experimental (or a low-energy) spin 3 (1,0,0) state. Keep the same for the four spin states 4 (-1,0,0) FANEDD, Research Program of Shanghai municipality and MOE. M.-H. W. thanks his surgeon Dr Thomas W. Maddox, MD, who provided him with the vital opportunity and time needed for writing this review.

D. Anisotropic spin exchange⁹⁵

Dalton Transactions

In some cases the spin exchange between two spin sites may not be isotropic. In such cases, one needs to examine its anisotropy. The anisotropic spin exchange interactions between two sites 1 and 2 can be written as

$$\hat{H} = J_{xx}\hat{S}_{1x}\hat{S}_{2x} + J_{yy}\hat{S}_{1y}\hat{S}_{2y} + J_{zz}\hat{S}_{1z}\hat{S}_{2z}$$
 (A16)

The values of J_{xx} , J_{yy} and J_{zz} can be determined on the basis of energy-mapping analysis by determining the energies of appropriate broken-symmetry spin states on the basis of DFT + U + SOC calculations.

(1) For J_{xx}^e :

$$J_{xx}^{e} = \frac{E_1 + E_4 - E_2 - E_3}{4} \tag{A17}$$

State	Spin 1	Spin 2	Other spin sites
1	(1, 0, 0)	(1, 0, 0)	Either $(0, 0, 1)$ or $(0, 0, -1)$ according to
2	(1, 0, 0)	(-1, 0, 0)	the experimental (or a low-energy) spin
3	(-1,0,0)	(1, 0, 0)	state. Keep the same for the four spin
4	(-1,0,0)	(-1, 0, 0)	states

(2) For $J_{\nu\nu}^e$:

$$J_{yy}^{e} = \frac{E_1 + E_4 - E_2 - E_3}{4} \tag{A18}$$

State	Spin 1	Cnin 0	Other spin sites
State	Spiii i	Spin 2	Other spin sites
1	(0, 1, 0)	(0, 1, 0)	Either $(0, 0, 1)$ or $(0, 0, -1)$ according to
2	(0, 1, 0)	(0, -1, 0)	the experimental (or a low-energy) spin
3	(0,-1,0)	(0, 1, 0)	state. Keep the same for the four spin
4	(0, -1, 0)	(0, -1, 0)	states

(3) For J_{zz}^e :

$$J_{zz}^{e} = \frac{E_1 + E_4 - E_2 - E_3}{4} \tag{A19}$$

State	Spin 1	Spin 2	Other spin sites
1	(0, 0, 1)	(0, 0, 1)	Either $(1, 0, 0)$ or $(-1, 0, 0)$ according to
2	(0, 0, 1)	(0, 0, -1)	the experimental (or a low-energy) spin
3	(0, 0, -1)	(0, 0, 1)	state. Keep the same for the four spin
4	(0, 0, -1)	(0, 0, -1)	states

Acknowledgements

The work at NCSU was supported by the computing resources of the NERSC center and the HPC center of NCSU. We would like to thank our colleagues Ms Jinhee Kang, Ms Jia Liu, Mr Jerry L. Bettis, Jr., Dr Chuan Tian, Dr Yuemei Zhang, Dr Won-joon Son, Dr Antoine Villesuzanne, Prof. Fang Wu and Prof. Erjun Kan. Work at Fudan was partially supported by NSFC, the Special Funds for Major State Basic Research,

References

- 1 M.-H. Whangbo, H.-J. Koo and D. Dai, *J. Solid State Chem.*, 2003, **176**, 417.
- 2 (a) R. G. Parr and W. Yang, Density-Functional Theory of Atoms and Molecules, Oxford University Press, 1989;
 (b) K. Capelle, arXiv:cond-mat/0211443v5 [cond-mat.mtrl-sci] 18 Nov 2006.
- 3 N. F. Mott, *Metal-Insulator Transitions*, Taylor & Francis, Ltd., 1974.
- 4 M.-H. Whangbo, J. Chem. Phys., 1979, 70, 4963.
- 5 (a) S. L. Dudarev, G. A. Botton, S. Y. Savrasov, C. J. Humphreys and A. P. Sutton, *Phys. Rev. B: Condens. Matter Mater. Phys.*, 1998, 57, 1505; (b) A. I. Liechtenstein, V. I. Anisimov and J. Zaanen, *Phys. Rev. B: Condens. Matter*, 1995, 52, 5467.
- 6 E. Bousquet and N. Spaldin, Phys. Rev. B: Condens. Matter, 2010, 82, 220402(R).
- 7 A. D. Becke, J. Chem. Phys., 1993, 98, 1372.
- 8 C. T. Lee, W. Yang and R. G. Parr, Phys. Rev. B, 1988, 37, 785.
- 9 J. Heyd, G. E. Scuseria and M. Ernzerhof, *J. Chem. Phys.*, 2003, **118**, 8207.
- 10 A. Stroppa and G. Kresse, *Phys. Rev. B: Condens. Matter Mater. Phys.*, 2009, **79**, 201201(R).
- 11 Y. G. Shi, Y. F. Guo, S. Yu, M. Arai, A. A. Belik, A. Sato, K. Yamaura, E. Takayama-Muromachi, H. F. Tian, H. X. Yang, J. Q. Li, T. Varga, J. F. Mitchell and S. Okamoto, *Phys. Rev. B: Condens. Matter Mater. Phys.*, 2009, **80**, 161104.
- 12 J. Kang, C. Lee and M.-H. Whangbo, in preparation.
- 13 W. J. Padilla, D. Mandrus and D. N. Basov, *Phys. Rev. B: Condens. Matter*, 2002, **66**, 035120.
- 14 W.-J. Son and M.-H. Whangbo, in preparation.
- 15 J. C. Slater, Phys. Rev., 1951, 82, 538.
- 16 J. S. Smart, *Effective Field Theory of Magnetism*, Saunders, Philadelphia, 1966.
- 17 G. L. Squires, *Introduction to the Theory of Thermal Neutron Scattering*, Cambridge University Press, 1978.
- 18 P. J. Hay, J. C. Thibeault and R. Hoffmann, J. Am. Chem. Soc., 1975, 97, 4884.
- 19 D. C. Mattis, The Theory of Magnetism, vols. I and II, Springer-Verlag, New York, 1987.
- 20 P. W. Anderson, Phys. Rev., 1959, 115, 2.
- 21 L. Noodleman, J. Chem. Phys., 1981, 74, 5737.
- 22 L. Noodleman and E. R. Davidson, Chem. Phys., 1986, 109, 131.
- 23 H. J. Xiang, E. J. Kan, S.-H. Wei, M.-H. Whangbo and X. G. Gong, *Phys. Rev. B: Condens. Matter Mater. Phys.*, 2011, 84, 224429.
- 24 (a) D. Dai and M.-H. Whangbo, J. Chem. Phys., 2001, 114, 2887; (b) D. Dai and M.-H. Whangbo, J. Chem. Phys., 2003, 118, 29.

- 25 (a) P. Rivero, I. de Pr Moreira and F. Illas, J. Phys.: Conf. Ser., 2008, 117, 012025; (b) I. de P. R. Moreira and F. Illas, Phys. Rev. B: Condens. Matter, 1997, 55, 4129; (c) I. de P. R. Moreira and F. Illas, Phys. Chem. Chem. Phys., 2006, 8, 1645.
- 26 J. W. Hong, A. Stroppa, J. Íñiguez, S. Picozzi and D. Vanderbilt, *Phys. Rev. B: Condens. Matter Mater. Phys.*, 2012, 85, 054417.
- 27 (a) G. Giovannetti, S. Kumar, A. Stroppa, J. van den Brink, S. Picozzi and J. Lorenzana, *Phys. Rev. Lett.*, 2011, **106**, 026401; (b) X. Rocquefelte, K. Schwarz and P. Blaha, *Phys. Rev. Lett.*, 2011, **107**, 239701.
- 28 J. B. Goodenough, *Magnetism and the Chemical Bond*, Interscience-Wiley, New York, 1963.
- 29 P. W. Anderson, Phys. Rev., 1950, 79, 350.

Perspective

- 30 B. J. Gibson, R. K. Kremer, A. V. Prokofiev, W. Assmus and G. J. McIntyre, *Phys. B*, 2004, **350**, e253.
- 31 D. Dai, H.-J. Koo and M.-H. Whangbo, *Inorg. Chem.*, 2004, 43, 4026.
- 32 H.-J. Koo, C. Lee, M.-H. Whangbo, G. J. McIntyre and R. K. Kremer, *Inorg. Chem.*, 2011, **50**, 3582.
- 33 Z. He, T. Kyômen and M. Itoh, *Phys. Rev. B: Condens. Matter Mater. Phys.*, 2004, **69**, 220407.
- 34 K. Ghoshray, B. Pahari, B. Bndyopadhyay, R. Sarkar and A. Ghoshray, *Phys. Rev. B: Condens. Matter Mater. Phys.*, 2005, 71, 214401.
- 35 H.-J. Koo and M.-H. Whangbo, *Inorg. Chem.*, 2006, 45, 4440.
- 36 C. Lee, J. Kang, K. H. Lee and M.-H. Whangbo, *Inorg. Chem.*, 2009, 48, 4185.
- 37 J. E. Greedan, *J. Mater. Chem.*, 2001, **11**, 37, and the references cited therein.
- 38 D. Dai and M.-H. Whangbo, *J. Chem. Phys.*, 2004, **121**, 672.
- 39 C. K. Majumdar and D. Ghosh, *J. Math. Phys.*, 1969, **10**, 1388.
- 40 D. Dai, H. J. Xiang and M.-H. Whangbo, *J. Comput. Chem.*, 2008, **29**, 2187.
- 41 H.-J. Koo, H. J. Xiang, C. Lee and M.-H. Whangbo, *Inorg. Chem.*, 2009, **48**, 9051.
- 42 N. D. Mermin and H. Wagner, *Phys. Rev. Lett.*, 1966, 17, 1133.
- 43 H. Kageyama, T. Watanabe, Y. Tsujimoto, A. Kitada, Y. Sumida, K. Kanamori, K. Yoshimura, N. Hayashi, S. Muranaka, M. Takano, M. Ceretti, W. Paulus, C. Ritter and G. André, *Angew. Chem.*, *Int. Ed.*, 2008, 47, 5740.
- 44 N. Hayashi, H. Kageyama, Y. Tsujimoto, T. Watanabe, S. Muranaka, T. Ono, S. Nasu, Y. Ajiro, K. Yoshimura and M. Takano, *J. Phys. Soc. Jpn.*, 2010, **79**, 123709.
- 45 Y. Tsujimoto, C. Tassel, N. Hayashi, T. Watanabe,
 H. Kageyama, K. Yoshimura, M. Takano, M. Ceretti,
 C. Ritter and W. Paulus, *Nature*, 2007, 450, 1062.
- 46 H. J. Xiang, S.-H. Wei and M.-H. Whangbo, *Phys. Rev. Lett.*, 2008, **100**, 167207.
- 47 (a) P. P. Ewald, Ann. Phys., 1921, 64, 253; (b) T. Darden,
 D. York and L. Pedersen, J. Chem. Phys., 1993, 98, 10089;

- (c) H. Wang, F. Dommert and C. Holm, *J. Chem. Phys.*, 2010, **133**, 034117.
- 48 S. T. Bramwell and M. J. P. Gingras, *Science*, 2001, 294, 1495, and the references cited therein.
- 49 N. W. Ashcroft and N. D. Mermin, *Solid State Physics*, Saunders College, Philadelphia, 1976, pp. 718–722.
- 50 (a) I. Dzyaloshinskii, J. Phys. Chem. Solids, 1958, 4, 241;(b) T. Moriya, Phys. Rev. Lett., 1960, 4, 228.
- 51 R. H. Buttner, E. N. Maslen and N. Spadaccini, *Acta Crystallogr., Sect. B: Struct. Sci.*, 1990, **46**, 131.
- 52 K. I. Kugel and D. I. Khomskii, *Sov. Phys. Usp.*, 1982, 25, 231.
- 53 C. Zerner, Phys. Rev., 1951, 82, 403.
- 54 R. D. Johnson, L. C. Chapon, D. D. Khalyavin, P. Manuel, P. G. Radaelli and C. Martin, *Phys. Rev. Lett.*, 2012, 108, 067201.
- 55 (a) X. Z. Lu, M.-H. Whangbo, S. A. Dong, X. G. Gong and H. J. Xiang, *Phys. Rev. Lett.*, 2012, 108, 187204;
 (b) J. H. Yang, Z. L. Li, X. Z. Lu, M.-H. Whangbo, S.-H. Wei, X. G. Gong and H. J. Xiang, *Phys. Rev. Lett.*, 2012, 109, 107203.
- 56 G. Ananthakrishna, L. F. Weiss, D. C. Foyt and D. J. Klein, *Physica*, 1976, **81B**, 275.
- 57 (a) F. Haldane, Phys. Lett. A, 1983, 93, 464; (b) F. Haldane, Phys. Rev. Lett., 1983, 50, 1153; (c) I. Affleck and E. H. Lieb, Lett. Math. Phys., 1986, 12, 57.
- 58 J. P. Renard, M. Verdaguer, L. P. Regnault, W. A. C. Erkelens, J. Rossat-Mignod and W. G. Stirling, Europhys. Lett., 1987, 3, 945.
- 59 L. W. Finger, R. M. Hazen and R. J. Hemley, Am. Mineral., 1989, 74, 952.
- 60 M. Jaime, V. F. Correa, N. Harrison, C. D. Batista, N. Kawashima, Y. Kazuma, G. A. Jorge, R. Stern, I. Heinmaa, S. A. Zvyagin, Y. Sasago and K. Uchinokura, *Phys. Rev. Lett.*, 2004, 93, 087203.
- 61 (a) M. Hase, M. Kohno, H. Kitazawa, N. Tsujii, O. Suzuki, K. Ozawa, G. Kido, M. Imai and X. Hu, *Phys. Rev. B: Condens. Matter Mater. Phys.*, 2006, 73, 104419; (b) M. Hase, M. Matsuda, K. Kakurai, K. Ozawa, H. Kitazawa, N. Tsujii, A. Dönni, M. Kohno and X. Hu, *Phys. Rev. B: Condens. Matter Mater. Phys.*, 2007, 76, 064431.
- 62 H.-J. Koo and M.-H. Whangbo, *Inorg. Chem.*, 2010, 49, 9253.
- 63 H. Ohta, S. Okubo, T. Kamikawa, T. Kunimoto, Y. Inagaki, H. Kikuchi, T. Saito, M. Azuma and M. Takano, J. Phys. Soc. Jpn., 2003, 72, 2464.
- 64 J. Kang, C. Lee, R. K. Kremer and M.-H. Whangbo, *J. Phys.: Condens. Matter*, 2009, 21, 392201.
- 65 M. Oshikawa, M. Yamanaka and I. Affleck, *Phys. Rev. Lett.*, 1997, 78, 1984.
- 66 F. E. Mapps and D. J. Machin, *Magnetism and Transition Metal Complexes*, Long Chapman and Hall, London, 1973.
- 67 X. Wang, R. Wu, D.-S. Wang and A. J. Freeman, *Phys. Rev. B: Condens. Matter*, 1996, 54, 61.
- 68 J. Kuneš, P. Novák, R. Schmid, P. Blaha and K. Schwarz, *Phys. Rev. B: Condens. Matter*, 2001, **64**, 153102.

69 M. Kenzelmann, A. B. Harris, S. Jonas, C. Broholm, J. Schefer, S. B. Kim, C. L. Zhang, S.-W. Cheong, O. P. Vajk and J. W. Lynn, Phys. Rev. Lett., 2005, 95, 087206.

Dalton Transactions

- 70 H. J. Xiang, S.-H. Wei, M.-H. Whangbo and J. L. F. Da Silva, Phys. Rev. Lett., 2008, 101, 037209.
- 71 S. Ji, E. J. Kan, M.-H. Whangbo, J.-H. Kim, Y. Oiu, M. Matsuda, H. Yoshida, Z. Hiroi, M. A. Green, T. Ziman and S.-H. Lee, Phys. Rev. B: Condens. Matter Mater. Phys., 2010, 81, 094421.
- 72 J. Liu, H.-J. Koo, H. J. Xiang, R. K. Kremer and M.-H. Whangbo, to be published.
- 73 J. P. Attfield, J. Phys.: Condens. Matter, 1989, 1, 7045.
- 74 M. G. Banks, R. K. Kremer, C. Hoch, A. Simon, B. Ouladdiaf, J.-M. Broto, H. Rakoto, C. Lee and M.-H. Whangbo, Phys. Rev. B: Condens. Matter Mater. Phys., 2009, 80, 024404.
- 75 C. Lee, H.-J. Koo, M.-H. Whangbo, R. K. Kremer and A. Simon, Phys. Rev. B: Condens. Matter Mater. Phys., 2012, 86,060407.
- 76 M. Herak, M. Miljak, G. Dhalenne and A. Revcolevschi, J. Phys.: Condens. Matter, 2010, 22, 026006, and the references cited therein.
- 77 B. D. White, W. M. Pätzold and J. J. Neumeier, Phys. Rev. B: Condens. Matter Mater. Phys., 2010, 82, 094439, and the references cited therein.
- 78 W. M. Reiff, A. M. LaPointe and E. H. Witten, J. Am. Chem. Soc., 2004, 126, 10206.
- 79 D. Dai and M.-H. Whangbo, *Inorg. Chem.*, 2005, 44, 4407.
- 80 Y. Zhang, E. J. Kan, H. J. Xiang, A. Villesuzanne and M.-H. Whangbo, *Inorg. Chem.*, 2011, **50**, 1758.
- 81 K. Takubo, T. Mizokawa, S. Hirata, J.-Y. Son, A. Fujimori, Topwal, D. D. Sarma, S. Rayaprol E.-V. Sampathkumaran, Phys. Rev. B: Condens. Matter Mater. Phys., 2005, 71, 073406.

- 82 H. Wu, M. W. Haverkort, Z. Hu, D. I. Khomskii and L. H. Tjeng, Phys. Rev. Lett., 2005, 95, 186401.
- 83 Y. Zhang, H. J. Xiang and M.-H. Whangbo, Phys. Rev. B: Condens. Matter Mater. Phys., 2009, 79, 054432.
- 84 C. Lee, E. J. Kan, H. J. Xiang, R. K. Kremer, S.-H. Lee, Z. Hiroi and M.-H. Whangbo, Inorg. Chem., 2012, 51, 6890.
- 85 Y. Tsukamoto, Y. Okamoto, K. Matsuhira, M.-H. Whangbo and Z. Hiroi, J. Phys. Soc. Jpn., 2011, 80, 094708.
- 86 J.-S. Lee, S. Ji and S.-H. Lee, private communication.
- 87 N. Emery, E. J. Wildman, J. M. S. Skakle, A. C. Mclaughlin, R. I. Smith and A. N. Fitch, Phys. Rev. B: Condens. Matter Mater. Phys., 2001, 83, 144429.
- 88 (a) J. Sólyom, Phys. Rev. B, 1987, 36, 8642; (b) P. Novák, I. Chaplygin, G. Seifert, S. Gemming and R. Laskowski, Comput. Mater. Sci., 2008, 79, 44; (c) A. Furrer, F. Juranyi, K. W. Krämer and Th. Strässle, Phys. Rev. B: Condens. Matter Mater. Phys., 2008, 77, 174410.
- 89 A. Marcinkova, T. C. Hansen, C. Curfs, S. Margadonna and J.-W. G. Bos, Phys. Rev. B: Condens. Matter Mater. Phys., 2010, 82, 174438.
- 90 H.-J. Koo, R. K. Kremer and M.-H. Whangbo, J. Phys. Soc. Jpn., 2012, 81, 063704.
- 91 F. Wu, E. J. Kan and M.-H. Whangbo, Inorg. Chem., 2010, 49, 3025.
- 92 H.-J. Koo and M.-H. Whangbo, Inorg. Chem., 2008, 47,
- 93 H.-J. Koo and M.-H. Whangbo, *Inorg. Chem.*, 2008, 47, 128.
- 94 C. Tassel, J. Kang, C. Lee, O. Hernandez, Y. Qiu, W. Paulus, B. Lake, T. Guidi, M.-H. Whangbo, H. Kageyama and S.-H. Lee, Phys. Rev. Lett., 2010, 105, 167205.
- 95 Z. L. Li, J. H. Yang, G. H. Chen, M.-H. Whangbo, H. J. Xiang and X. G. Gong, Phys. Rev. B: Condens. Matter Mater. Phys., 2012, 85, 054426.